The Astrophysical Journal, 953:190 (22pp), 2023 August 20 https://doi.org/10.3847/1538-4357/acdd7a

Early Planet Formation in Embedded Disks (eDisk). VII. Keplerian Disk, Disk Substructure, and Accretion Streamers in the Class 0 Protostar IRAS 16544–1604 in CB 68

Miyu Kido[1], Shigehisa Takakuwa[1,2], Kazuya Saigo[1], Nagayoshi Ohashi[2], John J. Tobin[3], Jes K. Jørgensen[4], Yuri Aikawa[5], Yusuke Aso[6], Frankie J. Encalada[7], Christian Flores[2], Sacha Gavino[4], Itziar de Gregorio-Monsalvo[8], Ilseung Han[6,9], Shingo Hirano[5], Patrick M. Koch[2], Woojin Kwon[10,11], Shih-Ping Lai[2,12,13,14], Chang Won Lee[6,9], Jeong-Eun Lee[15], Zhi-Yun Li[16], Zhe-Yu Daniel Lin[16], Leslie W. Looney[7], Shoji Mori[17], Suchitra Narayanan[18], Adele L. Plunkett[3], Nguyen Thi Phuong[6,19], Jinshi Sai (Insa Choi)[2], Alejandro Santamaría-Miranda[8], Rajeeb Sharma[4], Patrick D. Sheehan[3], Travis J. Thieme[12,13,14], Kengo Tomida[17], Merel L. R. van 't Hoff[20], Jonathan P. Williams[18], Yoshihide Yamato[5], and Hsi-Wei Yen[2]

[1] Department of Physics and Astronomy, Graduate School of Science and Engineering, Kagoshima University, 1-21-35 Korimoto, Kagoshima, Kagoshima 890-0065, Japan; k3394334@kadai.jp
[2] Academia Sinica Institute of Astronomy & Astrophysics, 11F of Astronomy-Mathematics Building, AS/NTU, No.1, Sec. 4, Roosevelt Rd., Taipei 10617, Taiwan, R.O.C.
[3] National Radio Astronomy Observatory, 520 Edgemont Rd., Charlottesville, VA 22903 USA
[4] Niels Bohr Institute, University of Copenhagen, Øster Voldgade 5–7, DK-1350 Copenhagen K., Denmark
[5] Department of Astronomy, Graduate School of Science, The University of Tokyo, 7-3-1 Hongo, Bunkyo-ku, Tokyo 113-0033, Japan
[6] Korea Astronomy and Space Science Institute, 776 Daedeok-daero, Yuseong-gu, Daejeon 34055, Republic of Korea
[7] Department of Astronomy, University of Illinois, 1002 West Green St., Urbana, IL 61801, USA
[8] European Southern Observatory, Alonso de Cordova 3107, Casilla 19, Vitacura, Santiago, Chile
[9] Division of Astronomy and Space Science, University of Science and Technology, 217 Gajeong-ro, Yuseong-gu, Daejeon 34113, Republic of Korea
[10] Department of Earth Science Education, Seoul National University, 1 Gwanak-ro, Gwanak-gu, Seoul 08826, Republic of Korea
[11] SNU Astronomy Research Center, Seoul National University, 1 Gwanak-ro, Gwanak-gu, Seoul 08826, Republic of Korea
[12] Institute of Astronomy, National Tsing Hua University, No. 101, Section 2, Kuang-Fu Rd., Hsinchu 30013, Taiwan
[13] Center for Informatics and Computation in Astronomy, National Tsing Hua University, No. 101, Section 2, Kuang-Fu Rd., Hsinchu 30013, Taiwan
[14] Department of Physics, National Tsing Hua University, No. 101, Section 2, Kuang-Fu Rd., Hsinchu 30013, Taiwan
[15] Department of Physics and Astronomy, Seoul National University, 1 Gwanak-ro, Gwanak-gu, Seoul 08826, Republic of Korea
[16] University of Virginia, 530 McCormick Rd., Charlottesville, VA 22904, USA
[17] Astronomical Institute, Graduate School of Science, Tohoku University, Sendai 980-8578, Japan
[18] Institute for Astronomy, University of Hawaii at Mānoa, 2680 Woodlawn Dr., Honolulu, HI 96822, USA
[19] Department of Astrophysics, Vietnam National Space Center, Vietnam Academy of Science and Techonology, 18 Hoang Quoc Viet, Cau Giay, Hanoi, Vietnam
[20] Department of Astronomy, University of Michigan, 1085 S. University Ave., Ann Arbor, MI48409-1107, USA
Received 2023 March 7; revised 2023 June 9; accepted 2023 June 9; published 2023 August 17

Abstract

We present observations of the Class 0 protostar IRAS 16544–1604 in CB 68 from the "Early Planet Formation in Embedded Disks (eDisk)" ALMA Large program. The ALMA observations target continuum and lines at 1.3 mm with an angular resolution of ∼5 au. The continuum image reveals a dusty protostellar disk with a radius of ∼30 au seen close to edge-on and asymmetric structures along both the major and minor axes. While the asymmetry along the minor axis can be interpreted as the effect of the dust flaring, the asymmetry along the major axis comes from a real nonaxisymmetric structure. The $C^{18}O$ image cubes clearly show the gas in the disk that follows a Keplerian rotation pattern around a ∼0.14 $M_{\odot}$ central protostar. Furthermore, there are ∼1500 au scale streamer-like features of gas connecting from northeast, north–northwest, and northwest to the disk, as well as the bending outflow as seen in the ^{12}CO (2–1) emission. At the apparent landing point of the NE streamer, there is SO (6_5–5_4) and SiO (5–4) emission detected. The spatial and velocity structure of the NE streamer can be interpreted as a free-falling gas with a conserved specific angular momentum, and the detection of the SO and SiO emission at the tip of the streamer implies the presence of accretion shocks. Our eDisk observations have unveiled that the Class 0 protostar in CB 68 has a Keplerian-rotating disk with a flaring and nonaxisymmetric structure associated with accretion streamers and outflows.

Unified Astronomy Thesaurus concepts: Star formation (1569); Interstellar medium (847); Planet formation (1241)

Supporting material: figure set

1. Introduction

There is now growing observational evidence that planet formation is initiated in circumstellar disks around protostars in their deeply embedded (Class 0/I) stages. For example, the mass of the disks around Class II young stellar objects (YSOs), so-called protoplanetary disks, is low compared to the total mass of solids in exoplanet systems, which suggests that planet formation should happen earlier than the Class II stage (Tychoniec et al. 2018; Ward-Duong et al. 2018; Tychoniec et al. 2020). The concentric ring and gap features found in dust disks around Class II YSOs are thought be related to planet

Table 1
Observational Parameters

Project Code		2019.1.00261.L		2019.A.00034.S
Observing date	24 Aug. 2021	04 Oct. 2021	05 Oct. 2021	14 Jun. 2022
Number of antennas	50	45	46	42
Configuration		C-8		C-4
Phase center		($16^h57^m19^s.64$, $-16^d09^m23^s.9$) (ICRS)		
		Continuum Image Parameters		
Synthesized beam (robust = 0.0)		0.″036×0.″027 (P.A = 69°)		
Conversion factor (robust = 0.0)		1 Jy beam^{-1} = 24836 K		
Noise level (robust = 0.0)		21 μJy beam^{-1} = 0.5 K		

formation processes; e.g., the gaps reflect the orbits of protoplanets, and rings are possible growth sites of planetesimals (Partnership et al. 2015; Pinte et al. 2016; Andrews et al. 2018; Long et al. 2018). Consequently, it is of great interest to characterize the structures of disks around deeply embedded protostars and to investigate whether they also show ring-like structures as seen around Class II YSOs—or perhaps precursors to these.

The purpose of the Atacama Large Millimeter/submillimeter Array (ALMA) Large Program "Early Planet Formation in Embedded Disks (eDisk)" is to systematically characterize the structures of disks around a sample of 19 protostars in Class 0/I stages through high spatial resolution images of 1.3 mm continuum and line emission (Ohashi et al. 2023). Specific interests of the target sources of eDisk include (1) the presence or absence of a Keplerian-rotating disk, as well as its size and internal structure (Tobin et al. 2012, 2015, 2020; Sheehan et al. 2022); (2) spatial and velocity structure of the protostellar envelope, including the accretion streamers onto the disk, which are found in recent ALMA studies (Yen et al. 2014, 2019a; Pineda et al. 2020; Thieme et al. 2022); and (3) evolutionary stage of the sources in the context of planet formation. In this paper we present the eDisk results for the Class 0 protostar IRAS 16544–1604 embedded in the Bok globule CB 68, located in the southwestern outskirt of the Ophiuchus North region (Launhardt & Henning 1997; Launhardt et al. 1998, 2010). In our eDisk papers, we simply refer to the Class 0 protostar IRAS 16544–1604 as IRAS 16544. IRAS 16544, one of the Class 0 sources among the eDisk sample, has a bolometric temperature $T_{\rm bol} = 50$ K and bolometric luminosity $L_{\rm bol} = 0.89\ L_\odot$, which are reestimated using the archival photometric data by the eDisk team (see Ohashi et al. 2023, for details). Distance estimates to the ρ Ophiuchus region range from 160 pc (Chini 1981) to 119 ± 6 pc (Lombardi et al. 2008), the latter based on Hipparcos and Tycho parallax measurements. A recent Very Long Baseline Array parallax measurement yielded a distance of 137.3 ± 1.2 pc (Ortiz-León et al. 2017). The distance to the cloud region closest to IRAS 16544 in Ophiuchus North was reported to be 151^{+3}_{-5} pc by Zucker et al. (2020), who adopted an advanced method that combines stellar photometric data with parallax measurements. In this paper we adopt this distance of 151 pc determined within a ∼5% accuracy. IRAS 16544 drives an expansive bipolar outflow along the northwest-to-southeast direction at a position angle of ∼140°, where the northwestern outflow lobe is redshifted and the southeastern lobe is blueshifted (Wu et al. 1996; Vallée et al. 2000; Vallée & Fiege 2007). Recently, Imai et al. (2022) reported results for IRAS 16544 at a spatial resolution of ∼70 au from the ALMA Large Program "Fifty AU Study of the chemistry in the disk/envelope system of Solar-like protostars (FAUST)." They revealed the presence of a ∼1000 au scale infalling and rotating protostellar envelope in $C^{18}O$ and the existence of a velocity gradient on a smaller scale (∼100 au), potentially related to disk rotation, in $C^{18}O$, CH_3OH, and OCS. Compact emission of various complex organic molecules is also found, suggesting that IRAS 16544 harbors a hot corino.

We here report the ∼5 au resolution observations for IRAS 16544 from eDisk, revealing the presence of a protostellar disk in Keplerian rotation and accretion streamers from the larger-scale cloud to this disk for the first time. The paper is organized as follows: Section 2 describes eDisk observations of IRAS 16544 and the parameters of the imaging. Section 3.1 shows the results of the 1.3 mm dust continuum emission. Images and velocity structures of the ^{12}CO (2–1) emission are shown in Section 3.2, while those of the ^{13}CO (2–1) and $C^{18}O$ (2–1) emission are shown in Section 3.3. In Sections 4.1 and 4.2, we analyze the Keplerian disk and streamers in the envelope, respectively. We further discuss the nature of the streamers in Section 5.1 and an overall physical picture of the Class 0 protostellar system IRAS 16544 in Section 5.2. Section 6 summarizes our main results. Appendix A shows the moment maps of the SO, c-C_3H_2, and H_2CO lines and the channel maps of the SiO, CH_3OH, and DCN lines. The full set of the velocity channel maps of the CO isotopologue lines is presented in Appendix B.

2. ALMA Observations and Data Reduction

The IRAS 16544 data presented in this paper were taken from two observing projects: one from the ALMA large program eDisk (project code: 2019.1.00261.L; PI: N. Ohashi), and the other from the Director's Discretionary Time (DDT) program (project code: 2019.A.00034.S; PI: J. J. Tobin). The eDisk observations were conducted to achieve high-resolution (<0.″1) imaging. The DDT observation was made to supplement the eDisk observations with a more compact antenna configuration C-4, which is sensitive to extended structures of ∼5″. Details of these observations are summarized in Table 1. Hereafter we call the eDisk observations/data LB (long-baseline) observations/data and call the DDT observation/data SB (short-baseline) observation/data. The correlator setup included seven spectral windows (SPWs). Two SPWs have a bandwidth of 1.875 GHz to increase the continuum sensitivity, four SPWs have a bandwidth of 58.594 MHz to ensure a high enough velocity resolution of the main target lines, and the remaining one has a 937.5 MHz bandwidth for the ^{12}CO (2–1) line. Between the LB and SB observations a slight change of the correlator setting was made for the ^{13}CO

Table 2
Observed Molecular Lines

Molecule	Transition	Frequency (GHz)	E_u[a,b] (K)	A[b,c] (s^{-1})	n_{crit}[b,d] (cm^{-3})	Beam Size	Δv[e] (km s^{-1})	rms (mJy $beam^{-1}$)
^{12}CO	2–1	230.538	16.60	6.910×10^{-7}	1.1×10^{4}	0.″24 × 0.″18 (P.A. = 79°)	0.635	1.2
^{13}CO	2–1	220.399	15.87	6.038×10^{-7}	9.4×10^{3}	0.″24 × 0.″18 (P.A. = 81°)	0.167	2.5
$C^{18}O$	2–1	219.560	15.81	6.011×10^{-7}	9.3×10^{3}	0.″27 × 0.″20 (P.A. = 77°)	0.167	1.9
SO	6_5–5_4	219.949	35.0	1.335×10^{-4}	2.3×10^{6}	0.″27 × 0.″20 (P.A. = 77°)	0.167	2.4
SiO	5–4	217.105	31.26	5.197×10^{-4}	2.4×10^{6}	0.″25 × 0.″19 (P.A. = 79°)	1.34	0.7
DCN[f]	3–2	217.239	20.85	4.57×10^{-4}	3.7×10^{7}	0.″25 × 0.″19 (P.A. = 79°)	1.34	0.7
CH_3OH	4_2–3_1	218.440	45.5	4.686×10^{-5}	2.0×10^{7}	0.″25 × 0.″19 (P.A. = 79°)	1.34	0.6
c-C_3H_2	$6_{0,6}$–$5_{1,5}$	217.822	38.61	5.393×10^{-4}	4.5×10^{7}	0.″25 × 0.″19 (P.A. = 79°)	1.34	0.7
	$5_{1,4}$–$4_{2,3}$	217.940	35.42	4.023×10^{-4}	4.8×10^{7}	0.″25 × 0.″19 (P.A. = 79°)	1.34	0.6
	$5_{2,4}$–$4_{1,3}$	218.160	35.42	4.039×10^{-4}	4.8×10^{7}	0.″25 × 0.″19 (P.A. = 79°)	1.34	0.6
H_2CO	$3_{0,3}$–$2_{0,2}$	218.222	21.0	2.818×10^{-4}	2.6×10^{6}	0.″25 × 0.″19 (P.A. = 79°)	1.34	0.6
	$3_{2,2}$–$2_{2,1}$	218.476	68.1	1.571×10^{-4}	3.0×10^{6}	0.″35 × 0.″27 (P.A. = 78°)	1.34	0.6
	$3_{2,1}$–$2_{2,0}$	218.760	68.1	1.577×10^{-4}	3.4×10^{6}	0.″26 × 0.″20 (P.A. = 77°)	0.167	1.8

Notes.
[a] Upper-state energy of the line.
[b] From the LAMDA database (Schöier et al. 2005).
[c] Einstein A-coefficient.
[d] Critical density at $T_K = 20$ K, except for that of the SO and c-C_3H_2 lines, which adopt 60 and 30 K, respectively. Calculated from the Einstein A- and C-coefficients from the LAMDA database.
[e] Velocity resolution.
[f] E_u and A values are from the CDMS database (Müller et al. 2001, 2005; Endres et al. 2016). The C-coefficient of the HCN line is adopted.

(2–1) emission. Table 2 lists the detected molecular lines, along with angular and velocity resolutions and rms noise levels.

The delivered visibility data after the standard pipeline calibrations were further edited and self-calibrated with the Common Astronomy Software Applications (CASA) version 6.2.1. The continuum-only visibility data were extracted from the channels without spectral emission lines detected. The SB continuum visibility data were Fourier-transformed and CLEANed with the CASA task *tclean*, and the SB-only continuum image was made. Then, self-calibrations of the SB continuum data only were conducted. The phase-only self-calibration was first conducted with progressively shorter solution intervals, which improved the signal-to-noise ratio (S/N) until the solution interval of "int." The total number of the iteration was 6. Then, a single amplitude and phase self-calibration was conducted. Next, from the self-calibrated SB visibility data and the three LB visibility data, individual 1.3 mm continuum images were made. Through the two-dimensional Gaussian fitting to the images, the centroid positions of the continuum images were derived, and the alignment of the image center was applied to the visibilities. Then, phase-only self-calibrations of the combined SB+LB data were conducted. We found that while the first and second rounds of the phase-only self-calibration improved the S/N, the third round of the phase-only calibration at the intermediate solution interval worsened the S/N. Amplitude and phase self-calibration was thus not performed for the SB+LB data. The calibration tables and the image centering were applied to the line visibility data. A more comprehensive description of the data reduction process can be found in Ohashi et al. (2023), where the standard eDisk data reduction script for each source is also linked.

With the self-calibrated SB+LB data sets, the final 1.3 mm continuum image was made with the Briggs robust parameter of 0.0, which gives the best compromise between the spatial resolution and S/N (Figure 1). For the line imaging robust = 2.0, i.e., natural weighting, and *uv*-tapering at 2000 kλ are adopted, except for the LB-only position–velocity (PV) diagram shown in Figure 2(b), which adopts robust = 1.5 and *uv*-tapering of 2000 kλ. We also made line images with robust = 0.5 and the same *uv*-tapering. We found, however, that those higher-resolution line images show patchy features, presumably due to the more severe effect of the missing flux. We thus adopted robust = 2.0 and *uv*-tapering at 2000 kλ for the line imaging.

3. RESULTS

3.1. 1.3 mm Dust Continuum Emission

Figure 1(a) shows the 1.3 mm dust continuum image of IRAS 16544 at an angular resolution of 0.″036 × 0.″027 (5.4 au × 4.1 au) (P.A. = 69°). The 1.3 mm dust emission is elongated along northeast to southwest. The dust emission likely traces a protostellar disk close to edge-on. Previous ALMA observations of IRAS 16544 in the dust continuum emission could not resolve such an elongated structure in the vicinity of the protostar (Imai et al. 2022). Our high-resolution eDisk observations have resolved the elongated disk feature around the protostar IRAS 16544 for the first time. From a two-dimensional Gaussian fitting with the CASA task *imfit*, the deconvolved FWHM of the 1.3 mm continuum emission along the major × minor axes is derived to be 0.″207 × 0.″060 (31.3 au × 9.1 au) at a position angle of 45°, where the fitting region is set to include the entire emission extent down to 3σ. Assuming that the dust grains are settled to the midplane, the aspect ratio equals $\cos i$, where i is the inclination angle ($i = 0°$ means face-on) and i is estimated to be $\gtrsim$73°. Since the grains are not completely settled, this serves as a lower limit. The location of the emission centroid derived from the two-dimensional Gaussian fitting is (α_{ICRS}, δ_{ICRS}) = ($16^h57^m19\overset{s}{.}6428$, $-16^d09^m24\overset{s}{.}016$), which we regard as the position of the central protostar (crosses in Figure 1). The centroid position of the Gaussian is slightly (~0.″01) offset from

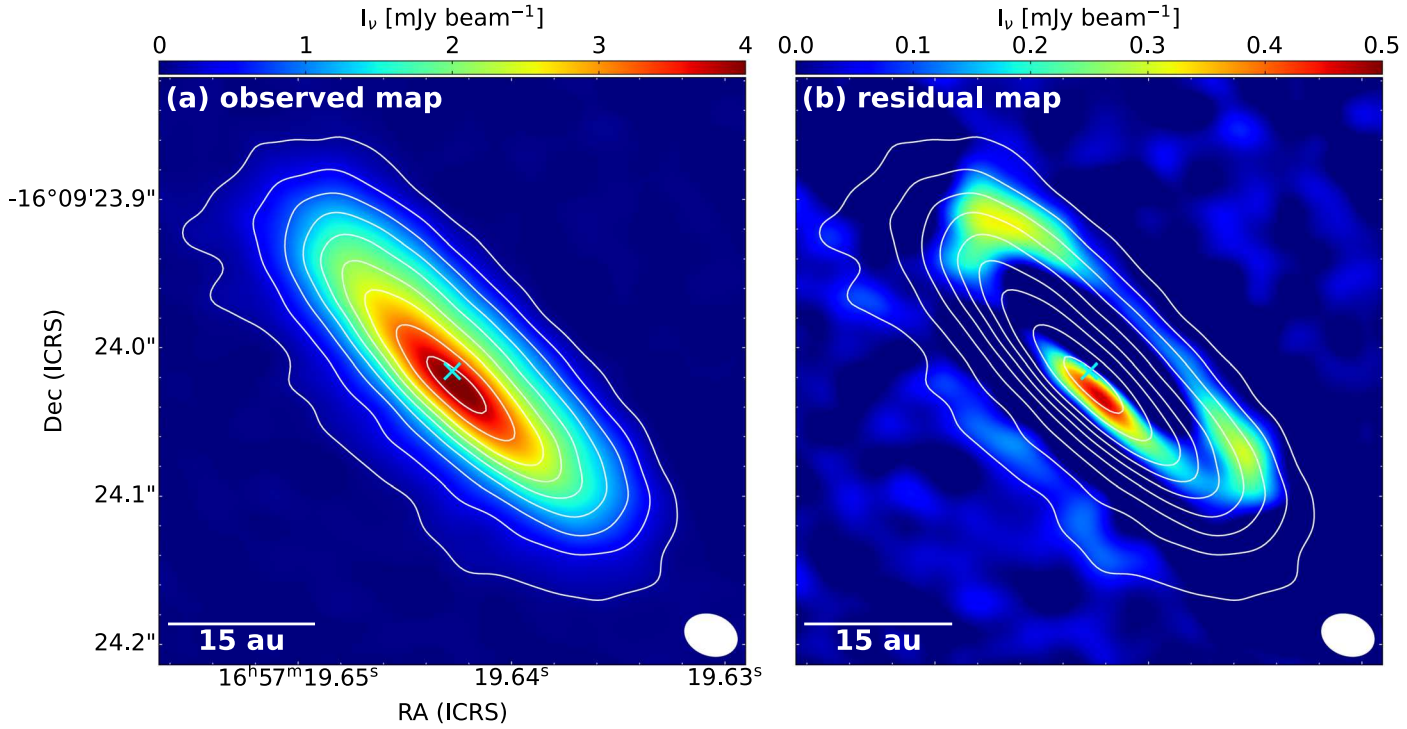

Figure 1. (a) 1.3 mm dust continuum image of IRAS 16544 with a robust parameter of 0.0. Contour levels are 5σ, 20σ, 40σ, 60σ, 80σ, 100σ, 120σ, 150σ, and 180σ ($1\sigma = 21$ μJy beam^{-1}). A cross at the center denotes the centroid position of the 1.3 mm dust continuum emission as derived from the two-dimensional Gaussian fitting, which is regarded as the protostellar position. A filled ellipse in the lower right corner shows the synthesized beam ($0\farcs036 \times 0\farcs027$; P.A. $= 69°$). (b) Residual 1.3 mm dust continuum image after subtracting the fitted two-dimensional Gaussian (color), overlaid with the observed image in white contours. Contour levels are the same as those in panel (a).

the position where the peak intensity of the map is seen. This reflects that the 2D Gaussian structure does not completely represent the actual intensity distribution as also illustrated in the residual map (Figure 1(b)) after subtracting the fitted Gaussian.

From the 1.3 mm flux density of 50.63 mJy ($\equiv S_\nu$) as derived from the integration over the emission area above 3σ, the dust mass of the disk ($\equiv M_{\rm dust}$) is calculated by the following formula:

$$M_{\rm dust} = \frac{S_\nu d^2}{\kappa_\nu B_\nu(T_{\rm dust})}, \quad (1)$$

where ν is the frequency ($= 225$ GHz), d is the distance ($= 151$ pc), κ_ν is the dust mass opacity, and $B_\nu(T_{\rm dust})$ is the Planck function at dust temperature $T_{\rm dust}$. The dust opacity of $\kappa_{225\ \rm GHz} = 2.3$ cm^2 g^{-1} is adopted (Beckwith et al. 1990). Adopting a typical value of the dust temperature in Class II disks, i.e., $T_{\rm dust} = 20$ K (Pascucci et al. 2016), $M_{\rm dust}$ is estimated to be $\sim$34.1 $M_\oplus$. Tobin et al. (2020) derived the scaling relation between the bolometric luminosity ($\equiv L_{\rm bol}$) and the dust temperature as

$$T_{\rm dust} = 43(L_{\rm bol}/L_\odot)^{1/4}\ {\rm K}. \quad (2)$$

For IRAS 16544, $T_{\rm dust}$ is estimated to be 42 K with $L_{\rm bol} = 0.89\ L_\odot$. This dust temperature gives $M_{\rm dust} \sim 14.1\ M_\oplus$. On the other hand, the peak brightness temperature of the dust emission is as high as 90 K (see Figure 3), suggesting that the dust temperature in the central region should be higher than 90 K. $T_{\rm dust} = 100$ K gives the dust mass of $M_{\rm dust} \sim 5.4\ M_\oplus$. Thus, with a fixed value of $\kappa_{225\ \rm GHz} = 2.3$ cm^2 g^{-1}, the range of the dust mass is $M_{\rm dust} \sim 5.4$–$34.1\ M_\oplus$. Assuming the gas-to-dust mass ratio of 100, this dust mass yields the total gas + dust mass of $1.63 \times 10^{-3}\ M_\odot$ to $1.02 \times 10^{-2}\ M_\odot$. Note that all of these estimates assume optically thin 1.3 mm dust emission. Since the high brightness temperature implies the optically thick 1.3 mm dust continuum emission at least partially, these mass estimates should be regarded as lower limits.

3.2. ^{12}CO (J = 2–1) Emission

Figure 4 shows various maps of the ^{12}CO (2–1) emission in IRAS 16544. From the analyses of the PV diagrams of the C^{18}O emission with the spectral line analysis/modeling (SLAM) code (see Section 4.1), the systemic velocity is derived to be 4.96 km s^{-1}, which is consistent with that in previous studies (Codella & Muders 1997; Imai et al. 2022). Hereafter in this paper we use $V_{\rm LSR} = 5.0$ km s^{-1} as a systemic velocity of IRAS 16544. Figures 4(a) and 4(b) compare the integrated-intensity maps of the blueshifted and redshifted ^{12}CO emission, while Figure 4(c) shows the moment 1 map. The ^{12}CO emission is predominantly distributed in a bipolar structure, normal to the elongated continuum structure, with the blueshifted and redshifted emissions located to the southeast and northwest, respectively. This distribution suggests that the ^{12}CO emission toward IRAS 16544 primarily traces the molecular outflow associated with the Class 0 protostar. There is also blueshifted emission toward the northwest and redshifted emission toward the southeast. This indicates that the outflow axis is close to the plane of the sky, which is consistent with the geometry of the dust disk close to edge-on ($i \gtrsim 73°$).

The redshifted outflow lobe to the northwest appears to consist of a number of jetlike emission components, which are most clearly visible in the peak intensity map (moment 8 map;

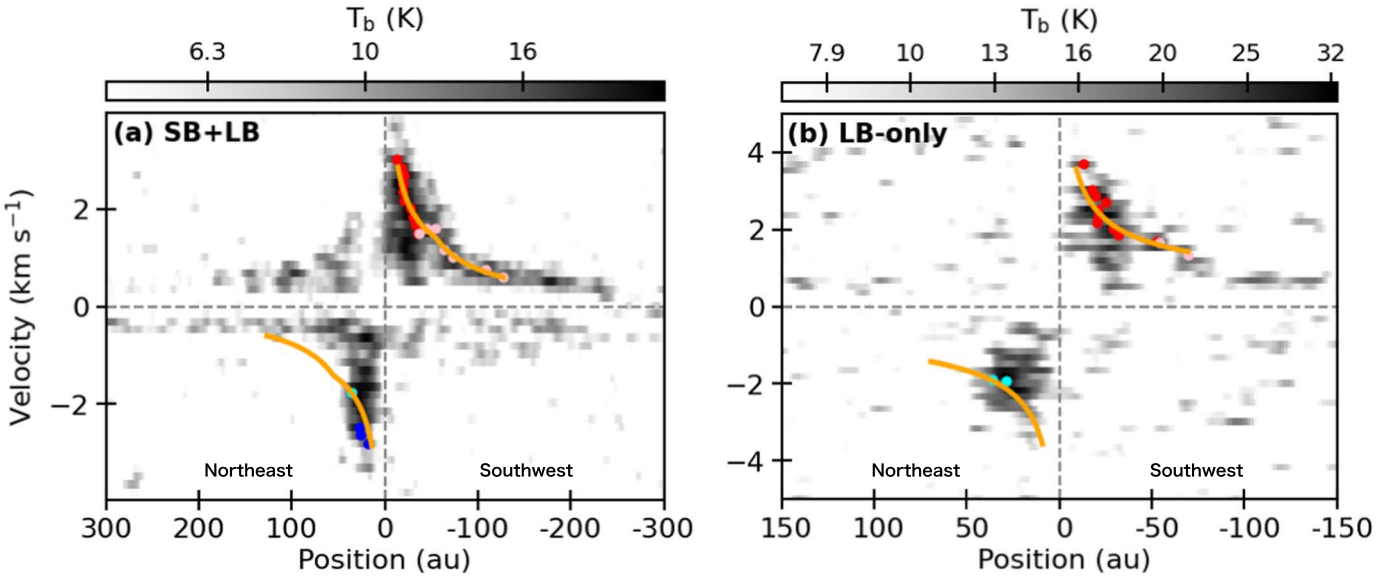

Figure 2. PV diagrams of the $C^{18}O$ (2–1) emission along the disk major axis (P.A. = 45°) using (a) the SB+LB data and (b) only the LB data. Blueish and reddish markers on the PV diagrams show the representative blueshifted and redshifted data points as derived from SLAM, and light and thick color markers denote the points derived from the profiles along the velocity and positional axes, respectively. Orange solid curves in panel (a) denote the result from the double power-law fitting of the rotational profile, while those in panel (b) denote the result from the single power-law fitting (see text for details).

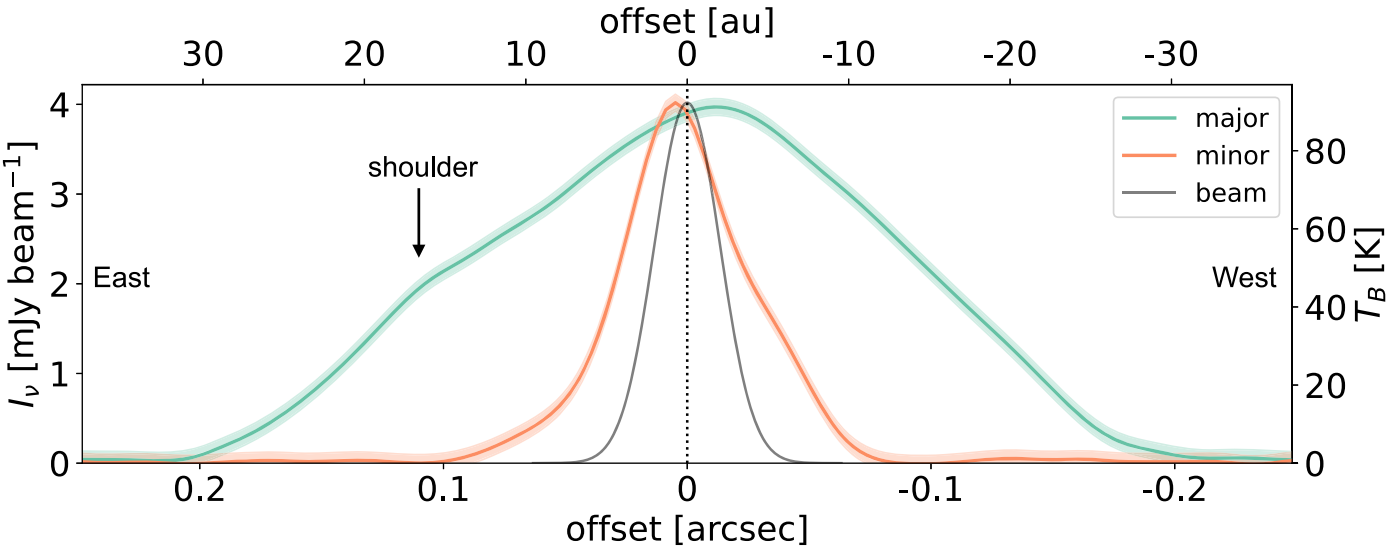

Figure 3. Intensity profiles of the 1.3 mm dust continuum emission along the major (light-green curve) and minor (orange) axes in IRAS 16544. The origin of the coordinates, denoted by a vertical dotted line, is set to be the centroid position of the continuum emission as derived from the two-dimensional Gaussian fitting. The positive direction of the major axis corresponds to northeast, and the positive direction of the minor axis corresponds to southeast. The right vertical axis indicates the brightness temperature. Shaded areas in the profiles denote the $\pm 3\sigma$ ranges. For comparison, the profile of the geometrically averaged beam is shown with a gray curve.

Figure 4(d)). These emission components point toward a variety of directions, suggesting that the outflow direction may have changed during the protostar's lifetime. From the visual inspection of the moment 0 map (Figure 4(b)), the mean position angle of the redshifted outflow lobe is derived to be $\sim -17°$. On the other hand, from the investigation of the ^{12}CO velocity channel maps we found that the ^{12}CO map at $V_{LSR} = 6.68$ km s^{-1} shows the V-shaped feature of the outflow cavity most unambiguously (Figure B1[21]). From this map the opening angle of the V shape is inferred to be $\sim 60°$ for a spatial extent of ~ 300 au at the outer intensity threshold of $\sim 50\sigma$, which corresponds the lowest contour level of the V-shaped cavity feature. The mean central axis of the redshifted outflow lobe appears to be tilted with respect to the minor axis of the dust disk (dashed line from northwest to southeast in Figure 4).

The blueshifted outflow lobe in contrast does not clearly exhibit such jetlike components toward different directions. The mean position angle of the blueshifted outflow is $\sim 135°$ from the visual inspection of Figure 4(a), which is not that of the redshifted lobe plus 180°. This suggests the presence of the outflow bending, which is also seen in other protostellar sources (e.g., Aso et al. 2018, 2019). If the magnetic field structure in a protostellar system is not orthogonal to the disk

[21] The full ^{12}CO velocity channel maps for the entire and zoom-in regions are available in the electronic journal.

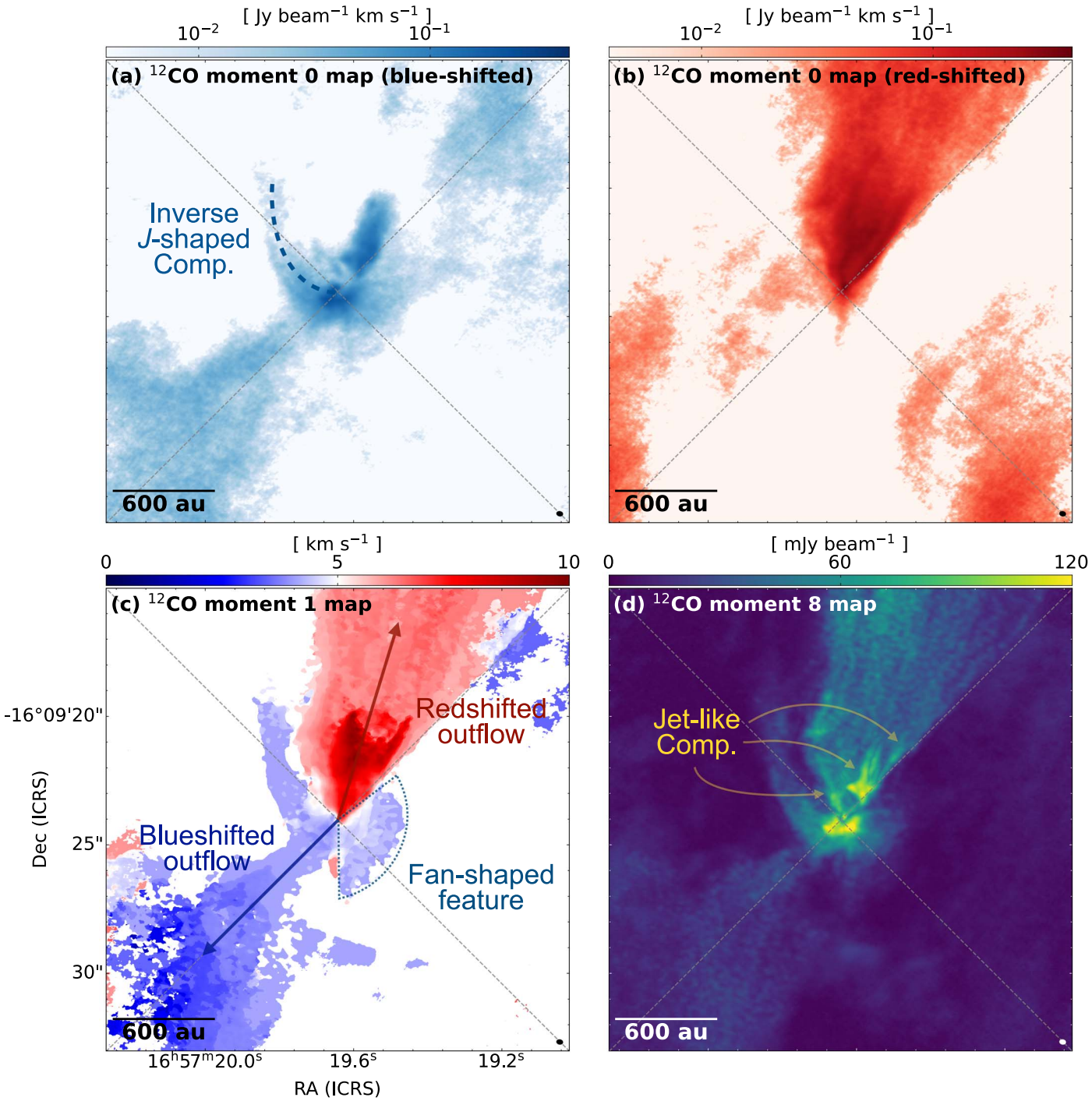

Figure 4. Various maps of the ^{12}CO (2–1) emission in IRAS 16544. (a, b) Moment 0 maps in the blueshifted ($V_{\rm LSR} = -2.21$ to 4.78 km s^{-1}) and redshifted ($V_{\rm LSR} =$ 5.41–23.19 km s^{-1}) velocity ranges. The color ranges from 4.0×10^{-3} Jy beam^{-1} km s^{-1} to 4.0×10^{-1} Jy beam^{-1} km s^{-1}. The apparent redshifted components to the southeastern and southwestern ends are interferometric artifacts. (c) Intensity-weighted mean velocity map (Moment 1 map). 10σ clipping is adopted to make this map ($1\ \sigma = 1.2$ mJy beam^{-1}). (d) Map of the peak intensity in the spectra (Moment 8 map). In all the panels, the gray dashed lines show the major and minor axes of the dust continuum image, and the filled ellipse in the lower right corner shows the synthesized beam. A blue dashed curve in panel (a) delineates the inverse-J-shaped feature.

rotational axis, misalignments between the outflow and disk rotational axes could be produced, and the observed bending outflow structure could reflect such a misalignment (e.g., Matsumoto & Tomisaka 2004; Hirano & Machida 2019; Hirano et al. 2020).

In addition to these outflow components, the ^{12}CO (2–1) emission also traces distinct components. There is an inverse-J-shaped blueshifted component (dashed curve in Figure 4(a)) starting from northeast from the protostar toward the southeastern end of the protostar. There is another, fan-shaped blueshifted component to the west of the protostar. Whereas the spatial distributions of these components appear to trace the shell surrounding the northern redshifted outflow, these components are blueshifted, and the velocity features of these components appear distinct from those of the outflows. In addition, these components have ^{13}CO and C^{18}O counterparts.

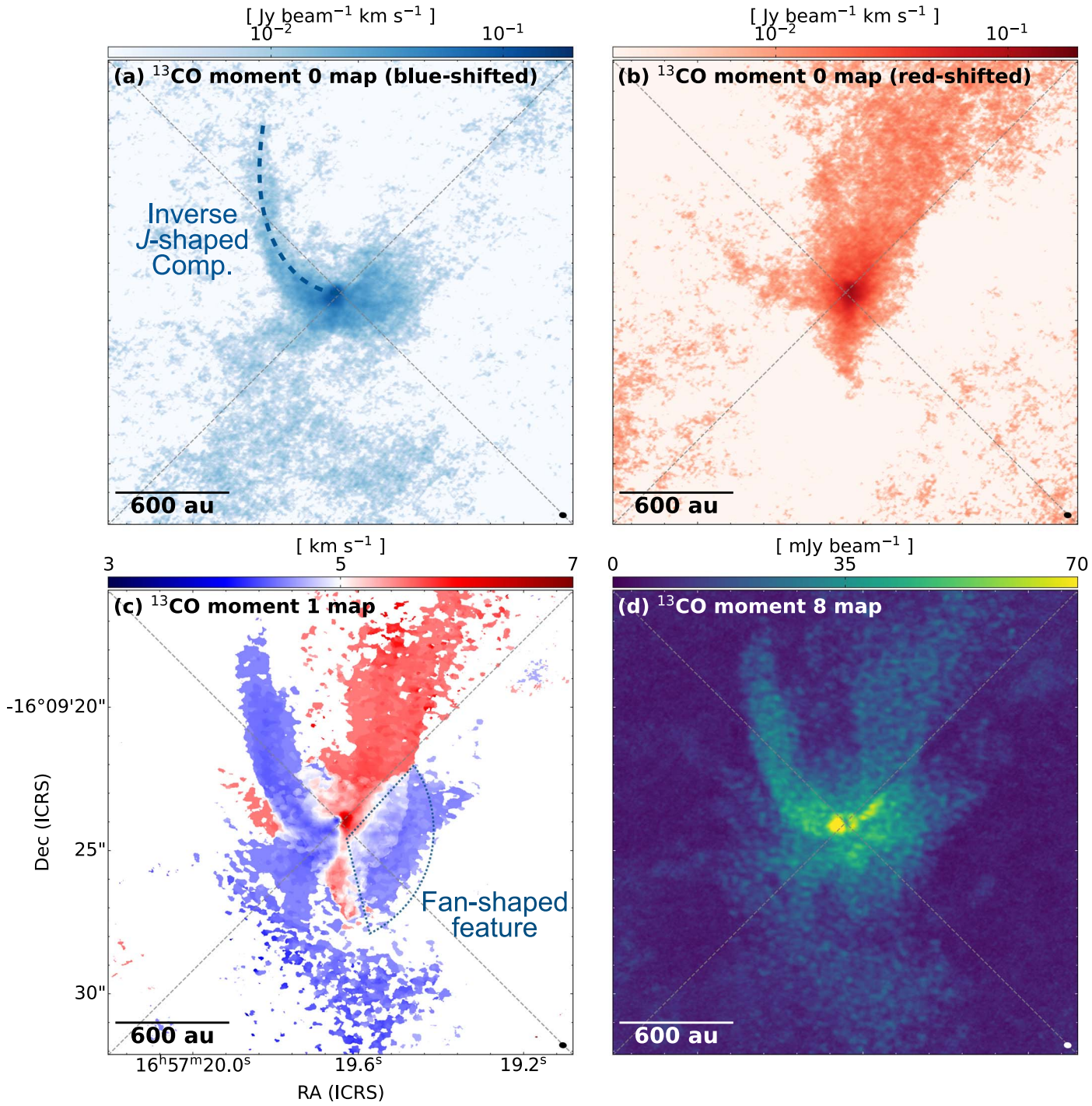

Figure 5. Same as Figure 4, but for the ^{13}CO (2–1) emission. The integrated velocity ranges of the moment 0 maps of the blueshifted and redshifted emission are $V_{\rm LSR} = 0.18$–4.85 km s^{-1} and 5.19–9.36 km s^{-1}, respectively. The color ranges from 2.0×10^{-3} Jy beam^{-1} km s^{-1} to 2.0×10^{-1} Jy beam^{-1} km s^{-1}. Here 5σ clipping is adopted to make the moment 1 map ($1\sigma = 2.5$ mJy beam^{-1}).

We will discuss the natures of these components in the subsequent sections.

3.3. ^{13}CO and C^{18}O (J = 2–1) Emission

Figures 5 and 6 show the ^{13}CO and C^{18}O counterparts of Figure 4. While the extended blueshifted and redshifted ^{13}CO and C^{18}O emission to the southeast and northwest, respectively, resembles the bipolar molecular outflow as traced by the ^{12}CO emission, the velocity structures of these components are distinct from those of the ^{12}CO outflows, as discussed below. Note that the velocity range of the ^{13}CO and C^{18}O emission is much narrower than that of the ^{12}CO emission. Furthermore, there is a blueshifted, inverse-J-shaped structure extending to the northeast (dashed curves in Figures 5 and 6). The same component is also seen in the ^{12}CO emission (Figure 4). There is another ^{13}CO and C^{18}O emission component located to the west of the protostar, which exhibits a blueshifted, fan-shaped feature. This component also has the ^{12}CO counterpart.

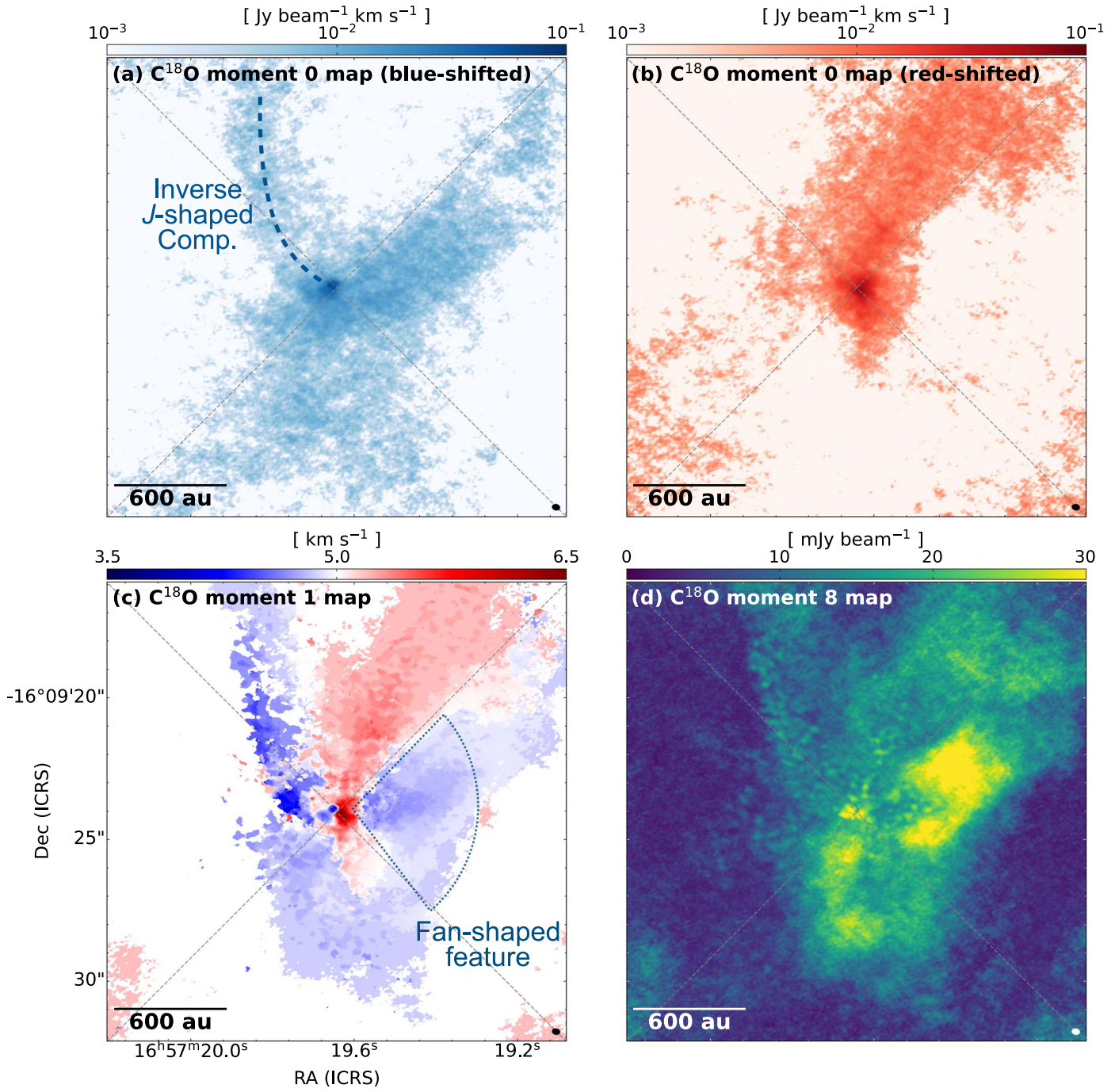

Figure 6. Same as Figure 4, but for the C^{18}O (2–1) emission. The integrated velocity ranges of the moment 0 maps of the blueshifted and redshifted emission are $V_{\rm LSR}$ = 1.18–4.85 km s^{-1} and 5.19–8.86 km s^{-1}, respectively. Here 5σ clipping is adopted to make the moment 1 map (1 σ = 1.9 mJy beam^{-1}).

The moment 0 and 1 maps of the CO isotopologue lines in the vicinity of the dust disk are shown in Figure 7. The ^{13}CO and C^{18}O emissions associated with the dust disk are visible, and in particular, the C^{18}O emission is elongated to the same direction as that of the dust emission (Figures 7(b) and (c)). This suggests that the C^{18}O emission traces the molecular gas in the protostellar disk. On the other hand, the ^{13}CO emission and particularly the ^{12}CO emission show more extended structures along the outflow direction, which may suggest that the ^{13}CO and ^{12}CO emissions have more contamination from the outflows. Inside the dust disk these CO isotopologue emissions are redshifted to the southwest and blueshifted to the northeast. This velocity gradient along the disk major axis can be interpreted as the rotational motion in the disk. On the contrary, outside the dust disk the CO isotopologue emission is red- and blueshifted to the northwest and southeast, respectively. In the ^{12}CO outflow map, the northwestern side is redshifted and the southeastern side blueshifted. Thus, the northwestern and southeastern sides of the disk correspond to the near and far sides of the disk plane, on the assumption that the disk plane is perpendicular to the outflow axis. If the ^{13}CO and C^{18}O components originate from the disk plane, the redshifted and blueshifted emissions arise from the near and far sides, and

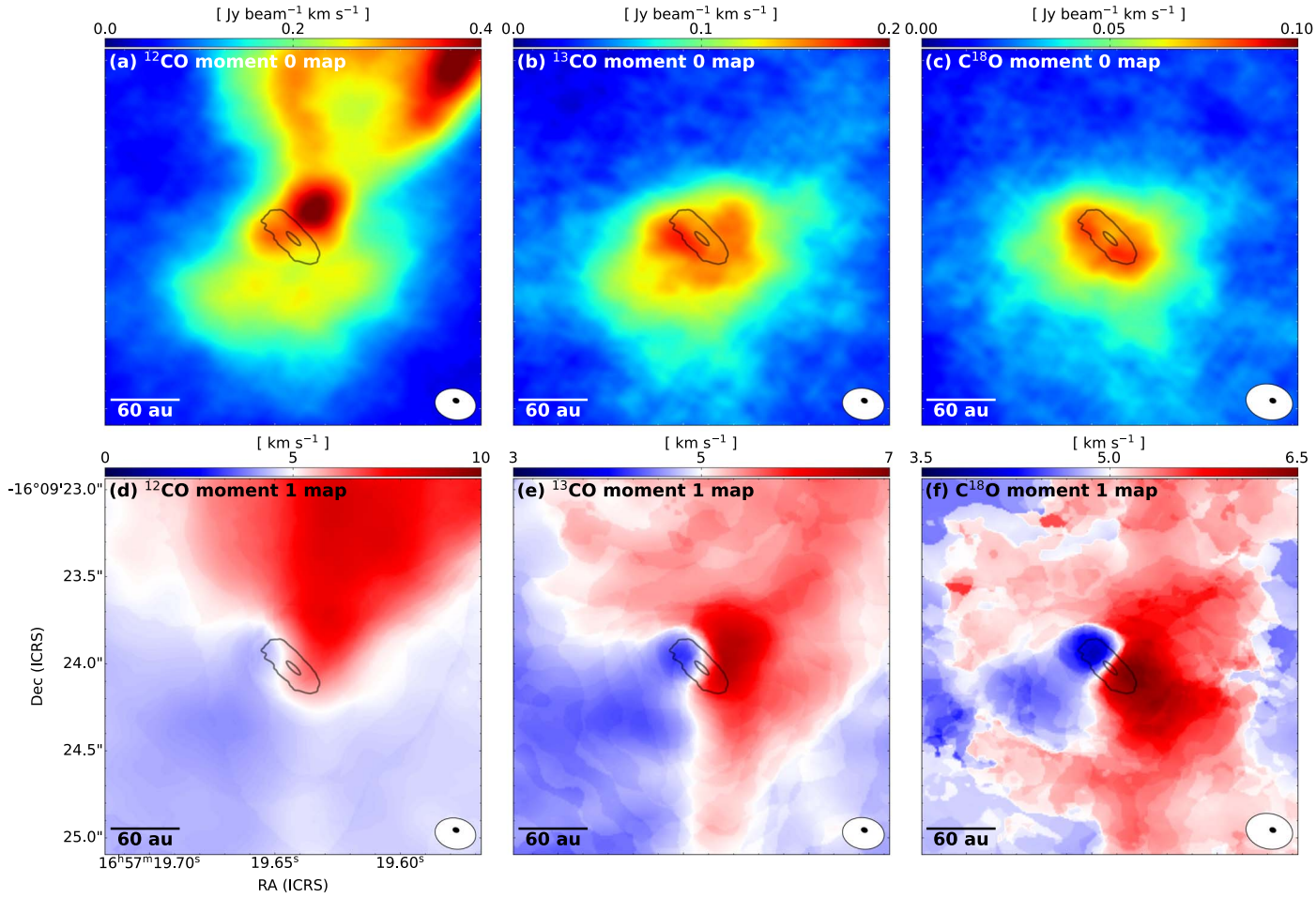

Figure 7. Moment 0 and 1 maps of the ^{12}CO, ^{13}CO, and C^{18}O (2–1) emission in the vicinity of the protostar as labeled. The integrated velocity ranges of the moment 0 maps are −12.37–23.19 km s^{-1}, 0.01–10.03 km s^{-1}, and 1.01–9.36 km s^{-1} for the ^{12}CO, ^{13}CO, and, C^{18}O emission, respectively. Here 5σ clipping is adopted to make moment 1 maps (1σ = 1.2, 2.5, and 1.9 mJy beam^{-1} for the ^{12}CO, ^{13}CO, and C^{18}O maps, respectively). Contours denote the 5σ and 150σ levels of the 1.3 mm continuum emission. White and black filled ellipses in the lower right corners denote the synthesized beams of the line and 1.3 mm continuum images, respectively.

such a velocity feature can be interpreted as an infalling motion.

To investigate the velocity features of the molecular gas surrounding the protostar in more detail, Figures 8 and 9 show the velocity channel maps of the C^{18}O emission in the high and low velocity ranges, respectively.[22] Note that the channel maps in the high velocity range are presented in the close vicinity of the dust disk (white contours in Figure 8). The high-velocity blueshifted C^{18}O emission is located to the northeastern part of the dust disk, while the high-velocity redshifted emission is located to the southwest, suggesting the presence of the velocity gradient along the disk major axis and rotation in the disk. In the blueshifted velocity range of 3.52–3.85 km s^{-1}, the location of the C^{18}O emission is shifted toward the southeast, which connects to the emission component in the lower blueshifted velocities shown in Figure 9. Similarly, in the redshifted velocity range of 6.19–6.52 km s^{-1}, the C^{18}O emission protrusion toward the west emerges, which connects to the lower redshifted emission in Figure 9.

The C^{18}O velocity channel maps at lower velocity ranges over the entire emission area (Figure 9) present gas components distinct from the central disk. At $V_{\rm LSR}$ = 4.02 km s^{-1}, a blueshifted component to the southeast of the disk is seen. From $V_{\rm LSR}$ = 4.19 km s^{-1}, a blueshifted, inverse-J-shaped structure emerges. This component curls from the southeast of the disk to the northeast and extends to the northeast progressively until $V_{\rm LSR}$ = 4.69 km s^{-1}. This velocity feature, that is, higher-velocity components located closer to the protostar and lower-velocity components located farther away, appears to be distinct from that of the outflows (see also Figure 10(b)). As we described above, this component is seen in all the CO isotopologue lines. In the velocity range of 4.19–4.69 km s^{-1}, there is another blueshifted component to the west of the protostellar disk. This component is the origin of the fan-shaped blueshifted signature seen in Figure 6. This western component also appears to curl to northwest and presents a similar spatial velocity feature to that of the northeastern blueshifted component, again opposite to that expected from the outflows. In the velocity range of 4.35–4.69 km s^{-1} the C^{18}O emission to the south is present. The extent of this blueshifted component is largest at the lowest velocity.

In the redshifted velocity of 6.02 km s^{-1}, the C^{18}O emission is located to the west of the protostar. In the lower redshifted velocities (5.35–5.86 km s^{-1}), this component appears to be divided into two components: one to the southwest of the disk,

[22] The full ^{13}CO and C^{18}O velocity channel maps for the entire and zoom-in regions are available in the electronic journal.

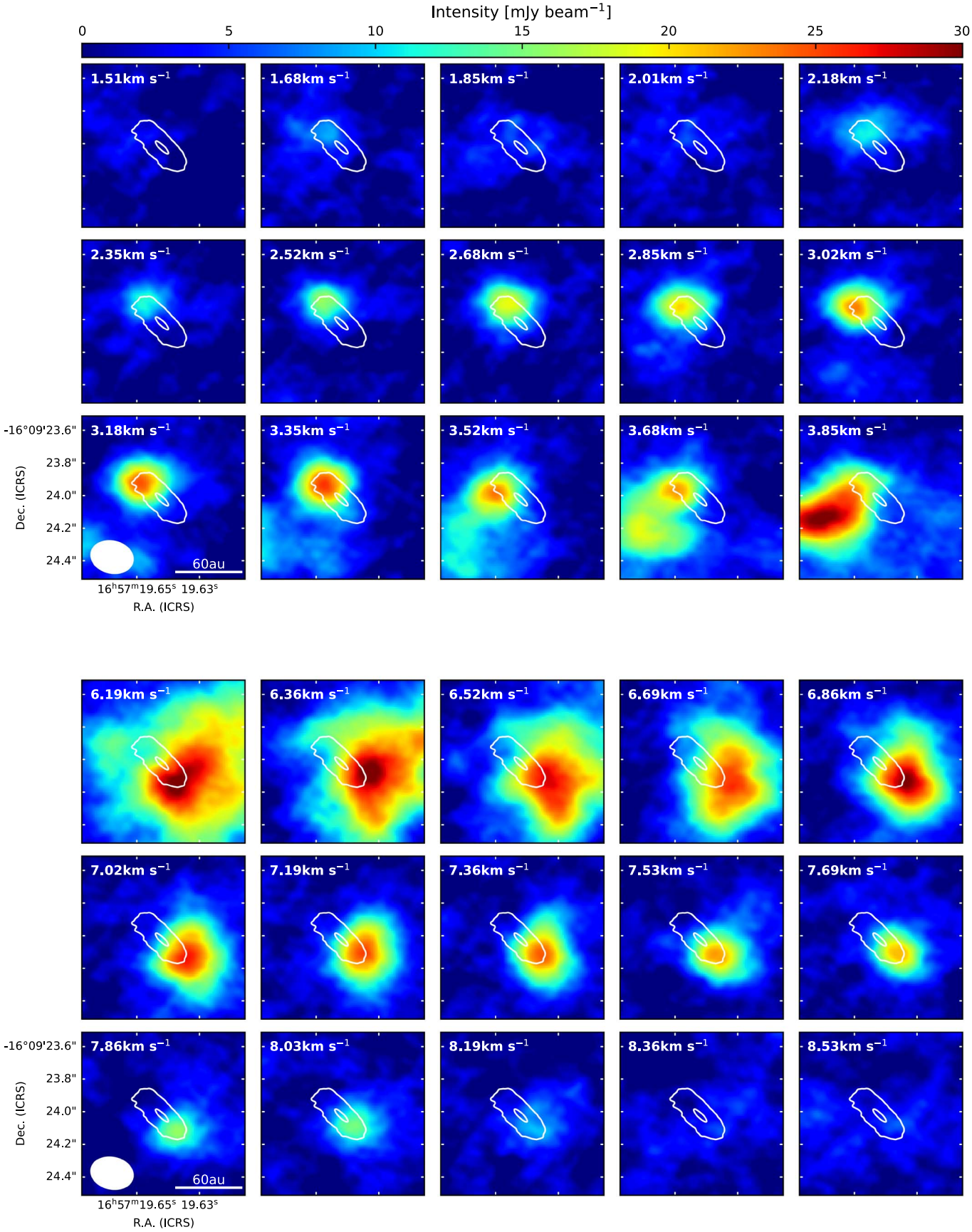

Figure 8. Channel maps of the $C^{18}O$ (2–1) emission in the high-velocity blueshifted (upper set of panels) and redshifted ranges (lower set of panels). Numbers in the upper left corners denote the LSR velocities. The systemic velocity is 5.0 km s^{-1}. Contours denote the distribution of the 1.3 mm continuum emission at 5σ and 150σ levels ($1\sigma = 21$ μJy beam^{-1}).

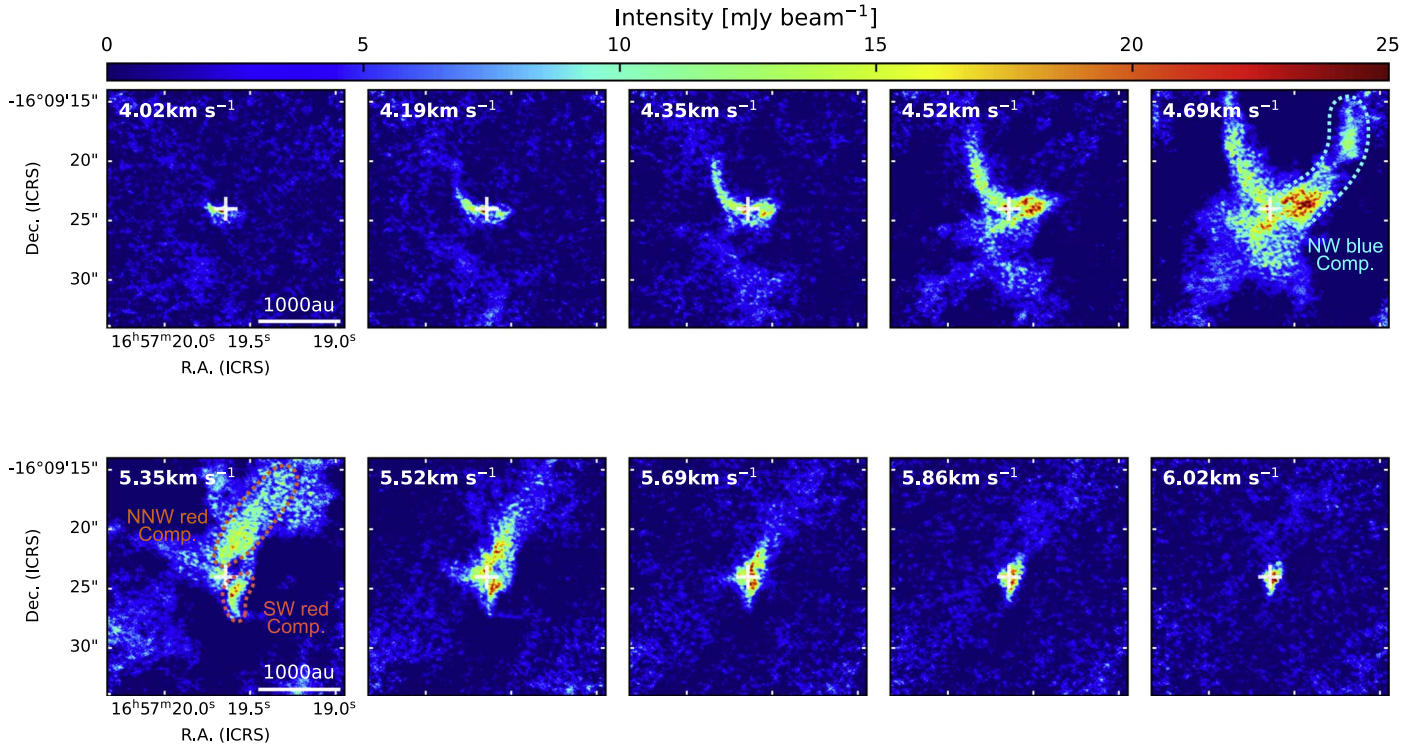

Figure 9. Channel maps of the $C^{18}O$ (2–1) emission in the low-velocity blueshifted (top panels) and redshifted ranges (bottom panels). Crosses show the position of the protostar, and numbers in the upper left corners denote the LSR velocities.

and the other extending to the north–northwest (NNW). While the spatial location of the NNW component matches with that of the redshifted outflow lobe as seen in the ^{12}CO emission, this component extends further to the NNW at lower velocities. A similar velocity feature of the redshifted ^{13}CO emission to the NNW is identified. The sense of this velocity structure seen in the $C^{18}O$ and ^{13}CO emission is opposite to that of the Hubble flow of molecular outflows (Arce et al. 2007).

4. Analysis

4.1. Keplerian Protostellar Disk

The CO isotopologue emission directly associated with the dust disk and most probably tracing the gas disk exhibits a velocity gradient along the northeast (blueshifted) to southwest (redshifted) direction. The velocity channel maps of the $C^{18}O$ (2–1) emission at high velocities (Figure 8) show archetypal signatures of the rotation. Figure 2 shows PV diagrams of the $C^{18}O$ (2–1) emission along the major axis of the dust disk (P.A. = 45°) using the SB+LB data (panel (a)) and the LB data only (panel (b)). The SB+LB and LB-only PV diagrams are made by averaging the spectra over the transverse width of 0.″15 and 0.″05, respectively. The SB+LB PV diagram shows the molecular emission not only in the first and third quadrants but also in the second and fourth quadrants. This result implies that the SB+LB PV diagram exhibits velocity structures of the protostellar disk, as well as those of the protostellar envelope. On the other hand, the LB-only PV diagram shows the emission predominantly in the first and third quadrants, suggesting that it traces the disk component only. Such a difference between the SB+LB and LB-only PV diagrams can be attributed to the different degree of the missing flux. In the high-velocity blueshifted and redshifted components (1 km s^{-1} $\leqslant$ $|V_{\rm LSR}-V_{\rm sys}|$ $\leqslant$ 3 km s^{-1}), the $C^{18}O$ emission is well separated to the northeast and southwest, respectively. On the other hand, at lower velocities ($|V_{\rm LSR} - V_{\rm sys}| \lesssim 1$ km s^{-1}) the SB+LB PV diagram shows overlaps of the northeastern and southwestern emission components at the same velocity. These results suggest that the high-velocity components trace the rotating disk, while the lower-velocity components correspond to the rotating and infalling protostellar envelope surrounding the disk as already demonstrated by the FAUST results (Imai et al. 2022).

Fitting of rotation curves to the $C^{18}O$ PV diagrams along the disk major axis was performed, using the SLAM code (Aso & Sai 2023). SLAM identifies an emission peak along each velocity or positional axis with the Gaussian fitting and derives the best parameters of the rotational profile, i.e., the central stellar mass ($\equiv M_\star$), the power-law index of the rotation velocity ($\equiv p$, where $v_{\rm rot} \propto r^{-p}$), and the outermost radius of the disk ($\equiv R_{\rm disk}$), through the Markov Chain Monte Carlo (MCMC) algorithm. The SLAM fitting to the emission ridge in the LB-only PV diagram with an intensity threshold of 3σ ($1\sigma = 2.0$ mJy beam^{-1}) indicates $p = 0.451 \pm 0.015$ and $R_{\rm disk} = 25.69 \pm 0.50$ au (solid orange curves in Figure 2(b)). The rotational power-law index is close to 0.5 of Keplerian rotation, which implies that the high-velocity $C^{18}O$ emission associated with the dust disk indeed traces the Keplerian rotation. The central protostellar mass is then derived to be $M_\star = 0.158 \pm 0.003\ M_\odot$. We note that these quoted errors are only statistical and arise from the MCMC process and that SLAM defines 68% of the posterior distribution as the range of the 1σ error. The actual error of the protostellar mass should be larger. For example, Czekala et al. (2015) adopted a more sophisticated fitting to the visibilities in the three-dimensional space and quoted 4% error bars on dynamical mass measurements of the pre-main-sequence spectroscopic binary AK Sco. Measurement of the dynamical mass of IRAS 16544

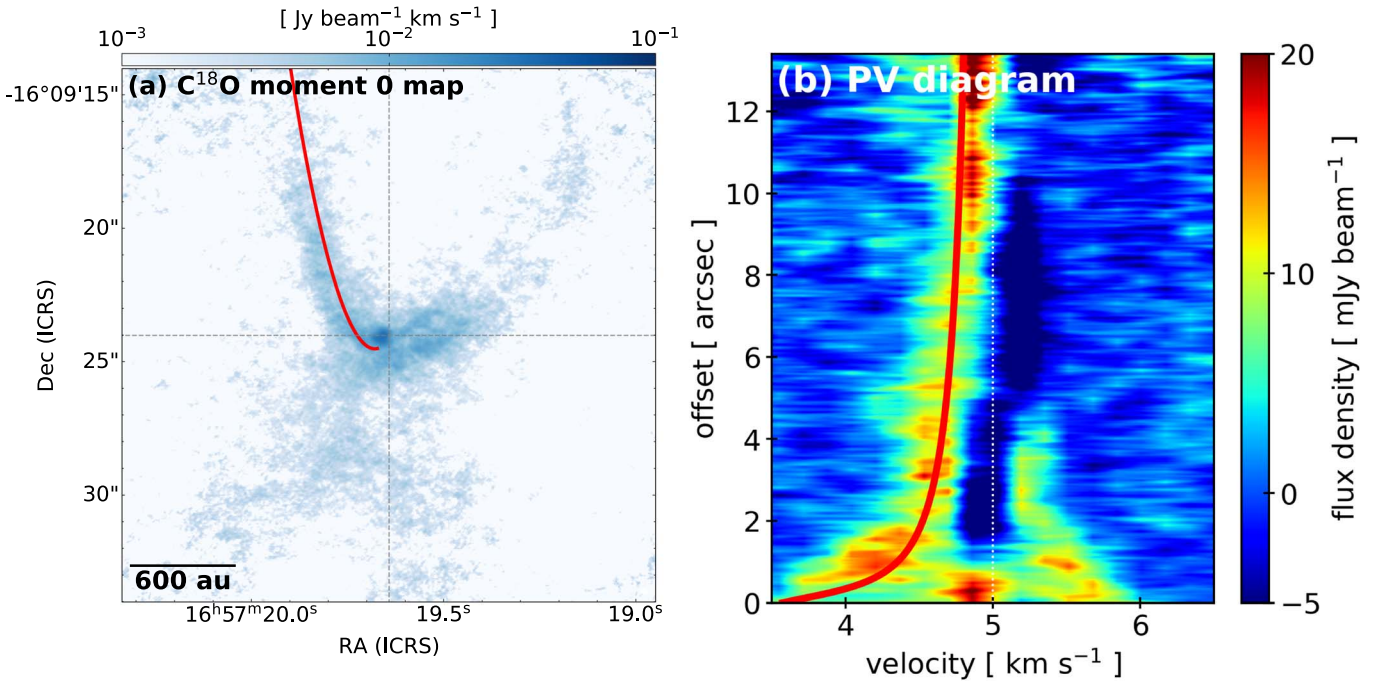

Figure 10. (a) Comparison of the solution of an accretion streamer to the spatial distribution of the NE streamer as seen in the moment 0 map of the $C^{18}O$ emission in the blueshifted velocity range (3.5–4.7 km s^{-1}). A red curve represents the solution at $\phi_0 = 64°$, $i_s = 73°$, and $\theta_s = 60°$, with a central stellar mass of 0.14 $M_\odot$ and a centrifugal radius of 100 au. (b) PV diagram of the $C^{18}O$ emission along the red curve shown in panel (a). A red curve shows a spatial and velocity trail of the accretion streamer shown in panel (a).

through such a full three-dimensional fitting is deferred to our next eDisk papers.

The SB+LB PV diagram, on the other hand, should include both the central Keplerian disk and the outer envelope. We thus adopted two rotational profiles using a double power-law function, i.e., the outer rotational profile in the envelope and the inner disk rotational profile. To avoid contamination from extended low-velocity gas, the fitting velocity range is restricted to 0.5 km s^{-1} $\leqslant |V_{\rm LSR}-V_{\rm sys}| \leqslant$ 4 km s^{-1}, and the intensity threshold of 5σ ($1\sigma = 1.3$ mJy beam^{-1}) is adopted. The double power-law fitting to the PV diagram with SLAM yields the power-law indices in the inner and outer regions of $p = 0.514 \pm 0.019$ and $p = 1.014 \pm 0.039$, respectively. The central protostellar mass is derived to be $M_\star = 0.137 \pm 0.003$ $M_\odot$, consistent with that from the LB-only fitting. The outermost disk radius, or the radius of the breaking point of the rotational profile, is derived to be $R_{\rm disk} = 54.55 \pm 0.50$ au. The larger disk radius as derived from the SB+LB data than that derived from the LB data only is likely attributed to the effect of the missing flux. Previous FAUST observations of IRAS 16544 have also derived the central stellar mass in the range of $M_\star = 0.08$–0.3 $M_\odot$, from the comparison of the PV diagram of a model infalling-rotating envelope to that of the observed $C^{18}O$ (2–1), CH_3OH (4_2–3_1 E), and OCS (19–18) emission. While this mass estimate is consistent with that of the present work, the FAUST estimate does not pinpoint the mass range and assumes that the protostellar envelope is free-falling, which is not necessarily the case (Takakuwa et al. 2013; Ohashi et al. 2014; Aso et al. 2015, 2017). Our higher-resolution eDisk observations have succeeded in resolving the disk structure and identifying the Keplerian rotation in the protostellar disk, which enables us to refine the value of the central protostellar mass.

4.2. Modeling of the Elongated Molecular Structure

In addition to the Keplerian protostellar disk, we have also identified intriguing elongated features at ∼1500 au scales seen in the lines of the CO isotopologues. The velocity channel maps of the $C^{18}O$ emission at low velocities (Figure 9) exhibit at least three such features: an inverse-J-shaped structure, a blueshifted component to the northwest of the disk, and a redshifted one extending to the NNW. The higher-velocity parts in these features are located closer to the protostar, which is opposite to the molecular outflow. Those high-velocity parts apparently deviate from the disk components as shown in Figures 8 and 9 at velocities of 3.52–3.85 km s^{-1} and 6.19–6.52 km s^{-1}. These features are reminiscent of accretion streamers recently observed in young, Class 0 protostars (e.g., Thieme et al. 2022).

We here discuss the spatial and velocity structure of the inverse-J-shaped structure to the northeast (hereafter we call this component the "NE streamer"). Figure 10(a) shows the moment 0 map of the NE streamer as seen in the $C^{18}O$ emission. A prominent inverse-J-shaped feature is evident in the moment 0 map. The PV diagram along the model curve that traces the emission ridge (see below) is shown in Figure 10(b). There appears to be a long chain of the $C^{18}O$ emission to the northeast of the source that is blueshifted, which we denote as the NE streamer. The NE streamer exhibits a gradual increase of the line-of-sight (LOS) velocity toward the central disk.

To reproduce these observational results, we calculated spatial and velocity trails of ballistic accretion based on the formulae by Ulrich (1976) and Cassen & Moosman (1981) (hereafter the CMU model). The radial ($\equiv v_r$) and azimuthal velocities ($\equiv v_\phi$) and the trail of the accretion are expressed as

$$v_r = -\left(\frac{GM_\star}{r}\right)^{1/2}(1-\cos\phi)^{1/2}, \quad (3)$$

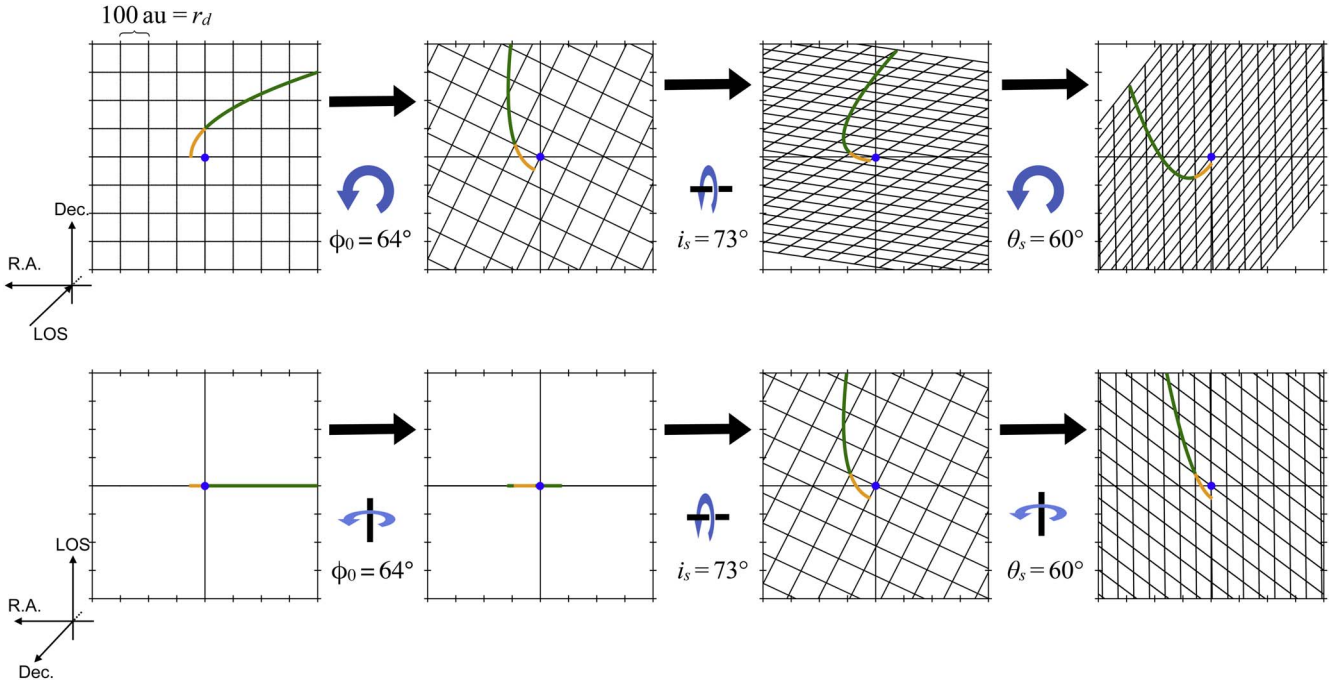

Figure 11. Top: illustrations of the streamer line projected on the plane of the sky. The *x*-, *y*-, and *z*-axes show R.A., decl., and the LOS, respectively. In the images one cell size corresponds to the centrifugal radius ($\equiv r_d = 100$ au). The blue and orange curves show the parabola outside/inside r_d, respectively. Filled blue circles show the position of the central protostar. From left to right, rotation around the parabola axis and rotation of the inclination and position angles are depicted for demonstration purposes. Bottom: top view of the spatial structure of the streamer. The *x*-, *y*-, and *z*-axes show R.A., LOS, and decl., respectively.

$$v_\phi = \left(\frac{GM_\star}{r}\right)^{1/2} (1 + \cos\phi)^{1/2}, \tag{4}$$

$$r = \frac{r_d}{1 + \cos\phi}, \tag{5}$$

where G is the gravitational constant, $M_\star$ is the mass of the central protostar, r is the radius, ϕ is the azimuth angle on the plane of the streamer, and r_d is the centrifugal radius. The mass of the central protostar is adopted as $M_\star = 0.14\ M_\odot$, which is derived from the SLAM fitting (see Section 4.1). We then varied r_d and ϕ_0, the incident azimuthal angle, as well as the inclination i_s and position angles θ_s of the rotational axis of the streamer, to match the observed spatial and velocity structures with the calculated trail by visual inspection. i_s is defined as the angle between the rotational axis and the LOS. ϕ_0 is the angle of the streamer to which the parabolic trajectory opens, and $\phi_0 = 0°$ indicates west when θ_s is 0° and increases counterclockwise. The visually determined parameter set is $\phi_0 = 64°$, $r_d = 100$ au, $i_s = 73°$, and $\theta_s = 60°$, with $M_\star = 0.14\ M_\odot$ (red curves in Figure 10). Illustration of the derived streamer line in the three-dimensional space is shown in Figure 11. Note that r_d is the parameter of the rotational angular momentum of the infalling material, and thus this can be different from the present radius of the disk toward which the materials are accreting. The calculated curve reproduces both the observed inverse-J-shaped feature and the gradual increase of the velocity as the position gets closer to the disk. This result implies that the NE streamer could be interpreted as an accretion streamer toward the central disk, although the curve in the PV diagram does not perfectly trace the observed spatial/velocity locations of the emission ridge.

5. Discussion

5.1. Accretion Streamer to the Protostellar Disk

From our model fitting in Section 4.2, it is likely that the NE elongated structure traces the trajectory of the material accreting to the disk. Figure 12 compares the spatial distribution of the NE streamer and the moment 0 maps of the SO (6_5–5_4) emission (panel (a)) and the SiO (5–4) emission (panel (b)) (contours) at the common velocity range. Figure 12 shows that the SO and SiO emission appears to trace the tip of the NE streamer. Furthermore, the SO and SiO emission appears to curl toward the northeast, following the trail of the NE streamer. Since the SO and SiO lines are known to be shocked gas tracers (Bachiller et al. 1998, 2001; Hirano et al. 2006; Sakai et al. 2014; Oya et al. 2018; Okoda et al. 2021), one of the possible interpretations for these emission distributions is that these emissions trace the accretion shock at the landing point of the streamer. The centrifugal radius of the NE streamer is estimated to be ~100 au (Section 4.2). This radius is larger than the radius of the Keplerian-rotating disk as inferred from the SLAM fitting (Section 4.1). Thus, the NE streamer is likely to accrete onto the envelope outside the Keplerian-rotating disk. A schematic picture of the streamer-plus-disk system is shown in Figure 13.

Previous ALMA observations of protostellar envelopes have also found similar accretion streamers. Yen et al. (2014) have revealed blueshifted (~2000 au in length) and redshifted (~5000 au) gas streamers in the $C^{18}O$ (2–1) emission toward the Class I protostar L1489 IRS. The blueshifted and redshifted streamers are found to accrete onto the plane of the large ($r \sim 300$ au) Keplerian protostellar disk above and below the disk plane, respectively. The velocity structures in these two steamers are consistent with free-falling gas flows with a

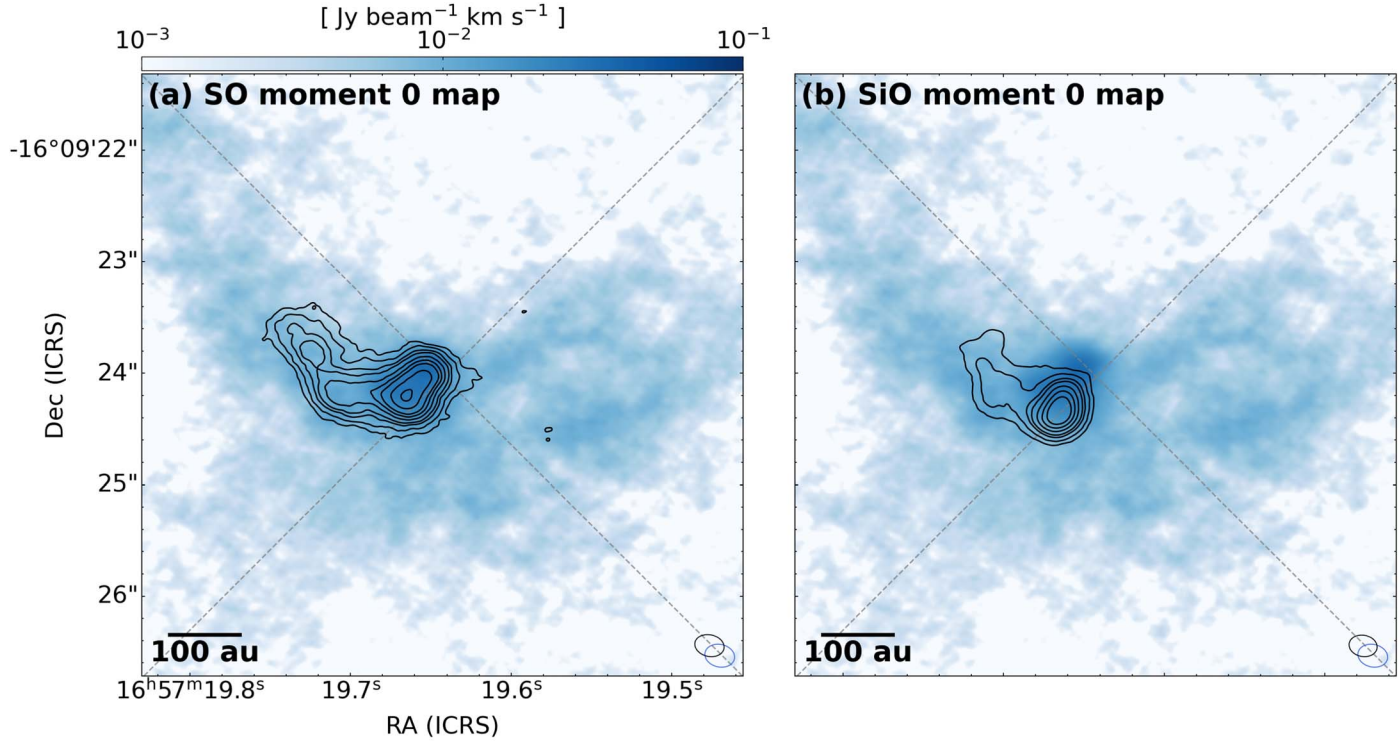

Figure 12. Comparison of the spatial distributions of the NE streamer as seen in the $C^{18}O$ (2–1) emission (colors) and the shock tracers of (a) SO (6_5–5_4) and (b) SiO (5–4) emission (contours). These shock tracers all peak to the southeast of the disk and might arise from the streamer's landing point. The integrated velocity ranges of the $C^{18}O$, SO, and SiO emission are 3.184–4.520 km s^{-1}, 3.184–4.520 km s^{-1}, and 3.18–4.52 km s^{-1}, respectively. Note that the SiO map is made from the integration over the two velocity channels at $V_{LSR} = 3.18$ and 4.52 km s^{-1} because of the coarser velocity resolution of the SiO data (=1.34 km s^{-1}). Contour levels are 5σ, 8σ, 12σ, 15σ, 20σ, 30σ, 40σ, 50σ, and 60σ (1σ = 1.2 and 1.3 mJy beam^{-1} km s^{-1} in panels (a) and (b), respectively). Blue and black open ellipses in the lower right corners denote the beam sizes of the $C^{18}O$ and the relevant molecular lines in the panels. The gray dashed lines are the same as in Figure 4.

centrifugal radius of 300 au and a mass accretion rate of (4–7) $\times 10^{-7}$ $M_\odot$ yr^{-1}. In HL Tau, Yen et al. (2019a) have found an intriguing one-arm spiral with a length of 520 au in the HCO^+ (3–2) emission, which extends from southwest to northwest of the planet-forming disk and curls toward the northwestern vicinity of the disk center. Kinematical analyses of this HCO^+ component reveal that the spiral is a rotating and infalling flow above the disk surface. In the Class 0 protostar Lupus 3-MMS, Thieme et al. (2022) found multiple extended accretion flows along the outflow cavities in the $C^{18}O$ (2–1) emission. The flows matched well with the CMU model with mass accretion rates of (0.5–1.1) $\times 10^{-6}$ $M_\odot$ yr^{-1}. While those flows follow the edges of the outflows, they have revealed that those structures are not outflow cavities but accretion flows, with the help of their kinematical model. Note that the streamer found in IRAS 16544 also resembles the outflow cavity at first glance. However, the channel map shows that the high-velocity component is detected near the central star and the low-velocity component is away from the IRAS 16544, suggesting that this component is not outflow related.

These growing pieces of evidence imply that accretion streamers in protostellar envelopes are not rare but could be a common astrophysical phenomenon. Recent high-resolution, high dynamic range observations of protostellar envelopes with ALMA have been finding these accretion streamers, which are in contrast with the classical picture that protostellar envelopes are continuous gas structures with rotation and infalling motions. If nonuniform, filamentary or fiber-like structures surround the natal dense cores (Hacar & Tafalla 2011; Hacar et al. 2013, 2017), it is natural that these gas structures exhibit accretion streamers in the course of protostellar formation. Numerical simulations of magnetized turbulent cloud cores indeed show such kinds of filamentary structures (Kuffmeier & Haugbølle 2017). Furthermore, a flattened envelope formed in the magnetized turbulent core is warped and exhibits spiral structures around a centrifugally supported rotating disk (Li et al. 2014). Nonideal MHD simulations with ambipolar diffusion also predict infalling spirals connecting to the central disk (Zhao et al. 2016, 2018).

5.2. *Physical Properties of the Disk Associated with the Class 0 Protostar IRAS 16544*

Our high-resolution eDisk observations have succeeded in identifying the Keplerian disk around the Class 0 protostar IRAS 16544. Previous interferometric observations have been finding a number of Keplerian-rotating disks around Class I protostars (e.g., Takakuwa et al. 2012; Yen et al. 2014; Aso et al. 2015; Yen et al. 2017), but only a handful of Class 0 protostars associated with the Keplerian disks are identified (e.g., Tobin et al. 2012; Murillo et al. 2013; Ohashi et al. 2014; Aso et al. 2017). A statistical study of Class 0 disks by CALYPSO argues that disk sizes around Class 0 sources could be smaller than those around Class I sources (see, e.g., Maury et al. 2019). ALMA observations of a Class 0 protostar B335 identified the upper limit of the radius of the Keplerian disk of $\lesssim$5 au (Yen et al. 2015, 2019b; Bjerkeli et al. 2019; Imai et al. 2019). Systematic studies of disk sizes as a function of the protostellar evolutionary sequence will be the subject of forthcoming eDisk papers.

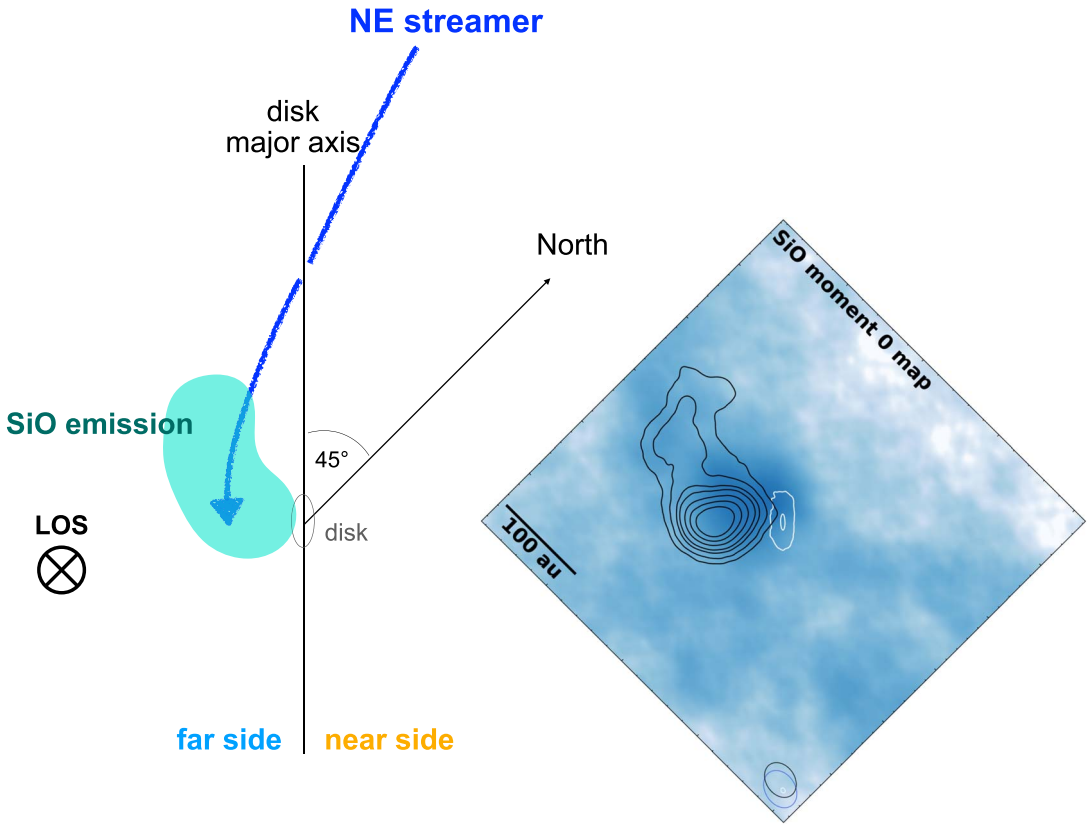

Figure 13. Schematic picture of the protostellar disk and the NE streamer in IRAS 16544 projected onto the plane of the sky obtained with the eDisk observations. For comparison, a zoom-in view of Figure 12(b), with the distribution of the dust continuum emission in white contours overlaid, is also shown aside. The contour levels of the continuum emission are 5σ and 150σ ($1\sigma = 21$ μJy beam^{-1}). The white ellipse in the lower right corner shows the beam size of the dust continuum emission.

The dust disk exhibits non-Gaussian, asymmetric structures, as shown in the residual image after the subtraction of the fitted Gaussian (Figure 1(b)). To investigate the distribution of the dust emission more closely, the intensity profiles of the 1.3 mm dust continuum emission along the major and minor axes are shown in Figure 3. The origin of the profiles is set to be the centroid position as derived from the Gaussian fitting. It is obvious that the Gaussian centroid does not match with the position of the emission peaks along both the major and minor axes. Along the major axis, the northeastern and southwestern parts are not mirror-symmetric, and there is a possible "shoulder" around $\sim 0\farcs11$ on the northeastern side. This may imply that the disk is not azimuthally symmetric. Along the minor axis, the peak location is $\sim 0\farcs01$ offset toward the southeast from the Gaussian centroid, and the northwestern profile is shallower than the southeastern profile within $\sim 0\farcs05$.

The observed peak brightness temperature of the 1.3 mm dust continuum emission exceeds $\gtrsim$90 K. While detailed radiative transfer modeling is required, such a high brightness temperature of the 1.3 mm dust continuum emission likely indicates that the 1.3 mm emission is optically thick. The observed outflows are redshifted to the northwest and blueshifted to the southeast, and thus the northwestern side of the dust disk is on the near side while the southeastern side is the far side. If the 1.3 mm dust continuum emission is optically thick and the dust distribution is flared, toward the southeastern, far side, the flared, warm disk surface is directly seen without the cold dust component intervening along the LOS. On the other hand, toward the northwestern, near side, we should see the colder portion of the disk close to the midplane along the LOS. Thus, the observed shift of the peak position of the 1.3 mm dust continuum emission along the minor axis can be interpreted as the disk flaring. Such a dust flaring has been directly imaged by the VLA observations of the optically thin 7 mm dust continuum emission toward the Class 0 protostar L1527 IRS by Sheehan et al. (2022).

Stability of a protostellar disk can be estimated with the Toomre Q parameter as

$$Q \sim \frac{2M_\star}{M_{\rm disk}} \frac{H}{R}, \tag{6}$$

where $M_{\rm disk}$ is the mass of the disk, $M_\star$ is the mass of the star, R is the radius, and H is the scale height at a radius R (e.g., Kratter & Lodato 2016; Tobin et al. 2020). From the results of the dust continuum emission and the SLAM fitting of IRAS 16544, we derived that $M_{\rm disk}$ is 1.63×10^{-3} $M_\odot$ to 1.02×10^{-2} $M_\odot$ and $M_\star$ is $\sim$0.14 $M_\odot$. Assuming the typical value of $\frac{H}{R} = 0.1$, the range of Toomre Q is 17–2.7. This nominal range of the Q value suggests that the protostellar disk is gravitationally stable. On the other hand, the 1.3 mm dust emission is probably optically thick as discussed above, and the derived disk mass should be regarded as a lower limit. If the true disk mass is several times higher, the protostellar disk should be gravitationally unstable. Observations at longer wavelengths, such as ALMA Band 1–3, are required to properly estimate the disk mass and the stability of the disk. If the true Q value is less than $\sim$1, the major-axis asymmetry and

the detected shoulder feature could be due to spirals induced by the gravitational instability.

Whereas the gravitational instability in a massive disk is a possible cause of the observed nonaxisymmetric dust feature, there are other physical mechanisms to produce such a disk asymmetry. In the case of IRAS 16544, the accretion streamers are observed, and the shock could affect the protostellar disk. The accretion shock can generate strong spiral density waves, which could exhibit the nonaxisymmetric feature in the disks (Lesur et al. 2015). Kuznetsova et al. (2022) have incorporated heterogeneous infall based on the CMU model and an embedded disk and performed hydrodynamic simulations to investigate the effect of the anisotropic accretion steamers on the disk structure. Their results demonstrate that the anisotropic infall induces the Rossby wave instability (RWI) in the disk and forms a vortex and azimuthally asymmetric feature in the disk. Recent growing observational evidence for accretion streamers, combined with this hydrodynamic simulation, implies that the streamers could be one of the main physical mechanisms to form the asymmetric structure in the disks. This in turn could affect future evolution of disks and planet formation therein. Within their parameter space, Kuznetsova et al. (2022) also argued that disk self-gravity does not play an important role, with the Toomre Q parameter above the marginal stability criterion. Another physical mechanism of formation of azimuthal asymmetric structure in the disk incorporates the presence of planetary and substellar companions. The companions in the disk can also induce RWI, vortex and gas horseshoes, and spiral density waves, which show asymmetric millimeter dust continuum emission (van der Marel et al. 2021).

IRAS 16544 is associated with an active, prominent molecular outflow. A rotating and infalling protostellar envelope has also been identified in IRAS 16544 (Imai et al. 2022), and we have found possible accretion streamers. These results suggest that IRAS 16544 is in the active mass accretion phase, typical of Class 0 sources. Our high-resolution eDisk observations have unveiled that such an active Class 0 protostar also has a well-developed Keplerian-rotating disk with hints of flaring and nonaxisymmetric substructure, which could be related to future planet formation in the disk.

6. Summary

We have carried out high-resolution ($0\farcs036 \times 0\farcs027 \sim 5$ au) and high-sensitivity ALMA observations of the young Class 0 protostar IRAS 16544–1604 embedded in Bok globule CB 68 with the 1.3 mm dust continuum emission, ^{12}CO, ^{13}CO, C^{18}O ($J = 2$–1), SO ($J_N = 6_5$–5_4), and other Band 6 lines as a part of the ALMA Large Program, eDisk. The main results are as follows:

1. The 1.3 mm dust continuum emission reveals an $r \sim 30$ au protostellar disk along the northeast-to-southwest direction at a position angle of ∼45°. The aspect ratio indicates that the disk is near to edge-on, with an inclination angle of ∼73°. Along the minor axis, the emission peak is skewed toward the southeast, and beyond the peak the emission profile is steeper on the southeastern side than on the northwestern side. The skewed intensity profile implies that the 1.3 mm dust continuum emission is optically thick and the dust distribution is flared, i.e., dusts are yet to be settled onto the midplane. The intensity profile along the major axis is not mirror-symmetric but asymmetric, with a possible shoulder ∼17 au to the northeast. This suggests the presence of nonaxisymmetric structure in this Class 0 protostellar disk.
2. The ^{12}CO (2–1) images show conspicuous molecular outflows, with the redshifted outflow lobe to the northwest and the blueshifted lobe to the southeast. The ^{12}CO emission in the redshifted lobe exhibits a number of flow-like features pointing in various directions. Furthermore, the axis of the redshifted outflow lobe appears not perpendicular to the disk, and the redshifted and blueshifted outflow lobes show a bending morphology. This could reflect misalignment between the magnetic fields and rotational axes in the natal core.
3. In the dust disk, the ^{12}CO, ^{13}CO, and C^{18}O (2–1) emissions are blueshifted to the northeast and redshifted to the southwest, which is interpreted as the rotation in the disk. Our analysis of the PV diagram of the C^{18}O emission along the disk major axis proves that the rotational profile is consistent with the Keplerian rotation, around a central protostar with a mass of ∼0.14 $M_\odot$.
4. In the outer region, the C^{18}O emission shows multiple streamer-like features. The most prominent one is an inverse-J-shaped, blueshifted component elongated toward the northeast (NE streamer), which has ^{12}CO and ^{13}CO counterparts. There are other such features: a redshifted component to the north–northwest, and a blueshifted one to the northwest. In these features, the higher-velocity components are located closer to the protostellar disk, suggesting accretion motion. We searched for the trajectory of the ballistic infalling flow that reproduces the moment 0 map and the PV diagram of the NE streamer. We found that a centrifugal barrier of 100 au reasonably reproduces the spatial and velocity structure of the NE streamer, with a central protostellar mass of 0.14 $M_\odot$ derived from the PV analysis of the Keplerian disk. Furthermore, the SO (6_5–5_4) and SiO (5–4) emissions, shock tracers, are seen at the tip of the NE streamer. Since the centrifugal radius of the NE streamer is larger than the radius of the Keplerian disk (∼50 au), the NE streamer is landing on the envelope outside the Keplerian-rotating disk, where the accretion shock takes place.

Our high-resolution eDisk observations of the Class 0 protostar IRAS 16544 have identified a compact Keplerian-rotating disk associated with flared and nonaxisymmetric dust distribution. At the same time, active mass outflow and mass accretion are ongoing through the powerful molecular outflows and accretion streamers, respectively. The nonaxisymmetric signature in the dust disk could reflect the spiral features induced by the gravitational instability in the disk, or interaction with the accretion streamers, although the optical thickness of the 1.3 mm dust continuum emission prevents us from directly investigating the disk mass and its gravitational stability. These results present an updated physical picture of the Class 0 stage, when formation of substructures often seen in Class II disks has started.

Acknowledgments

We are grateful to N. Harada and M. Omura for technical assistance with the Python codes. We would like to thank all the ALMA staff supporting this work. M.K. is supported by the ALMA Japan Research Grant of NAOJ ALMA Project, NAOJ-ALMA-292. S.T. is supported by JSPS KAKENHI grant Nos. 21H00048 and 21H04495 and by NAOJ ALMA Scientific Research grant No. 2022-20A. K.S. is supported by JSPS KAKENHI grant No. 21H04495. N.O. and C.F. acknowledge support from National Science and Technology Council (NSTC) in Taiwan through grants NSTC 109-2112-M-001-051 and 110-2112-M-001-031. J.J.T. acknowledges support from NASA RP 80NSSC22K1159. J.K.J. acknowledges support from the Independent Research Fund Denmark (grant No. 0135-00123B). Y.A. acknowledges support by NAOJ ALMA Scientific Research Grant code 2019-13B, Grant-in-Aid for Scientific Research (S) 18H05222, and Grant-in-Aid for Transformative Research Areas (A) 20H05844 and 20H05847. F.J.E. acknowledges support from NSF AST-2108794. S.G. acknowledges support from the Independent Research Fund Denmark (grant No. 0135-00123B). I.D.G.-M. acknowledges support from grant PID2020-114461GB-I00, funded by MCIN/AEI/10.13039/501100011033. P.M.K. acknowledges support from NSTC 108-2112-M-001-012, NSTC 109-2112-M-001-022, and NSTC 110-2112-M-001-057. W.K. was supported by the National Research Foundation of Korea (NRF) grant funded by the Korea government (MSIT) (NRF-2021R1F1A1061794). S.-P.L. and T.J.T. acknowledge grants from the NSTC of Taiwan 106-2119-M-007-021-MY3 and 109-2112-M-007-010-MY3. C.W.L. is supported by the Basic Science Research Program through the NRF funded by the Ministry of Education, Science and Technology (NRF-2019R1A2C1010851) and by the Korea Astronomy and Space Science Institute grant funded by the Korea government (MSIT; project No. 2022-1-840-05). J.-E.L. is supported by the NRF grant funded by the Korean government (MSIT; grant No. 2021R1A2C1011718). Z.-Y.L. is supported in part by NASA 80NSSC20K0533 and NSF AST-1910106. Z.-Y.D.L. acknowledges support from NASA 80NSSCK1095, the Jefferson Scholars Foundation, the NRAO ALMA Student Observing Support (SOS) SOSPA8-003, the Achievements Rewards for College Scientists (ARCS) Foundation Washington Chapter, the Virginia Space Grant Consortium (VSGC), and UVA research computing (RIVANNA). L.W.L. acknowledges support from NSF AST-2108794. S.M. is supported by JSPS KAKENHI grant Nos. JP21J00086 and 22K14081. S.N. acknowledges support from the National Science Foundation through the Graduate Research Fellowship Program under grant No. 2236415 and from NSF AST-2107841. R.S. acknowledges support from the Independent Research Fund Denmark (grant No. 0135-00123B). P.D.S. acknowledges support from NSF AST-2001830 and NSF AST-2107784. M. L.R.H. acknowledges support from the Michigan Society of Fellows. J.P.W. acknowledges support from NSF AST-2107841. Y.Y. is supported by the International Graduate Program for Excellence in Earth-Space Science (IGPEES), World-leading Innovative Graduate Study (WINGS) Program of the University of Tokyo. H.-W.Y. acknowledges support from the NSTC in Taiwan through grant NSTC 110-2628-M-001-003-MY3 and from the Academia Sinica Career Development Award (AS-CDA-111-M03). This paper makes use of the following ALMA data: ADS/JAO.ALMA #2019.1.00261.L and 2019.A.00034.S. ALMA is a partnership of ESO (representing its member states), NSF (USA), and NINS (Japan), together with NRC (Canada), NSTC and ASIAA (Taiwan), and KASI (Republic of Korea), in cooperation with the Republic of Chile. The Joint ALMA Observatory is operated by ESO, AUI/NRAO, and NAOJ. The National Radio Astronomy Observatory is a facility of the National Science Foundation operated under cooperative agreement by Associated Universities, Inc.

Software: CASA (McMullin et al. 2007), matplotlib (Hunter 2007), bettermoments (Teague & Foreman-Mackey 2018; Teague 2019), PVextractor (Ginsburg et al. 2016), APLpy (Robitaille & Bressert 2012; Robitaille 2019), SLAM (Aso & Sai 2023), astropy (Astropy Collaboration et al. 2022).

Facility: ALMA.

Appendix A
Spatial and Velocity Structures of the Detected Molecular Lines

The spectral setting of eDisk enables us to observe a number of ancillary molecular lines simultaneously (see Table 2). In this appendix, we present spatial and velocity structures of these molecular lines.

Figure A1 shows the moment 0, 1, and 8 maps of the SO ($J_N = 6_5$–5_4) emission in IRAS 16544. The primary SO emission peak is located to southeast of the dust disk, and the secondary peak is located to the northwest. Additional emission peaks are seen to the east and northeast of the primary peak, and these emission components likely comprise the blueshifted, the NE streamer seen in the CO isotopologue lines (see Figure A1(b)). On the other hand, the secondary SO peak to the northwest is redshifted. To the west of the protostar, an extended, fan-shaped redshifted SO emission is present. The blueshifted component to the west of the protostar as seen in the CO isotopologue lines (see Figure 9) is not seen in the SO emission, and the difference of the distributions between the SO and CO isotopologue emission in the three-dimensional space is present. This is the reason why the moment 1 map of the SO emission appears redshifted to the west while that of the CO isotopologue emission appears blueshifted.

Figures A2, A3, and A4 show velocity channel maps of the SiO (5–4), CH_3OH (4_2–3_1 E), and DCN (3–2) emission, respectively. In the blueshifted velocity of 3.18–4.52 km s^{-1}, the SiO emission peaks toward the southeast of the dust disk. At $V_{LSR} = 4.52$ km s^{-1}, the SiO emission distribution curls toward the northeast, consistent with our interpretation that the SiO emission traces the tip of the NE streamer. The SiO emission is also present on the southeastern side at the redshifted velocity $V_{LSR} = 5.86$ km s^{-1}. The CH_3OH emission is located toward the southeast of the disk, but the peak location is closer to the disk than that of the SiO emission. In addition, the CH_3OH emission shows a clear velocity gradient along the disk major axis, consistent with the disk rotation. Thus, the CH_3OH emission could originate from the protostellar disk. The DCN emission shows a similar emission component to the southeast with a velocity gradient along the disk major axis, while another redshifted component to the northwest is also seen.

Figure A5 compares the moment 0 maps of the three c-C_3H_2 and H_2CO lines. The c-C_3H_2 emissions are extended (~2000 au), and a number of patchy c-C_3H_2 emission components are present. The $6_{0,6}$–$5_{1,5}$ and $5_{1,4}$–$4_{2,3}$ transitions are weak toward the protostellar disk, while the $5_{2,4}$–$4_{1,3}$

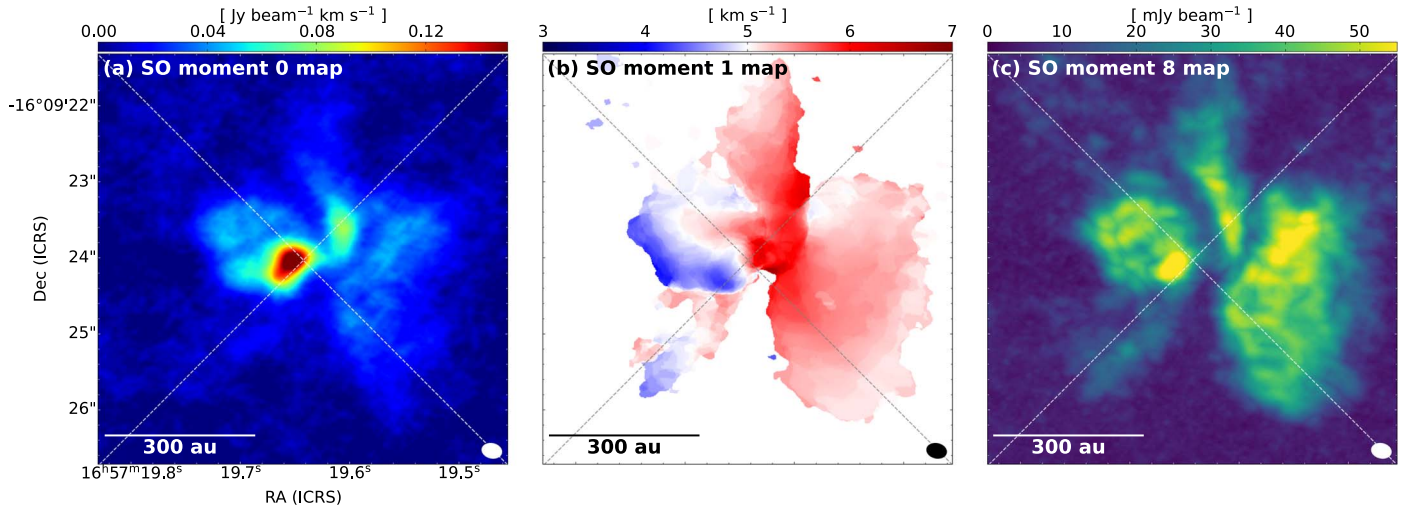

Figure A1. Moment 0, 1, and 8 maps of the SO (6_5–5_4) emission in IRAS 16544. The integrated velocity range of the moment 0 map is from 1.514 to 9.196 km s^{-1}. Here 5σ clipping is adopted to make the moment 1 map (1 $\sigma = 2.4$ mJy beam^{-1}). The white and gray dashed lines are the same as in Figure 4.

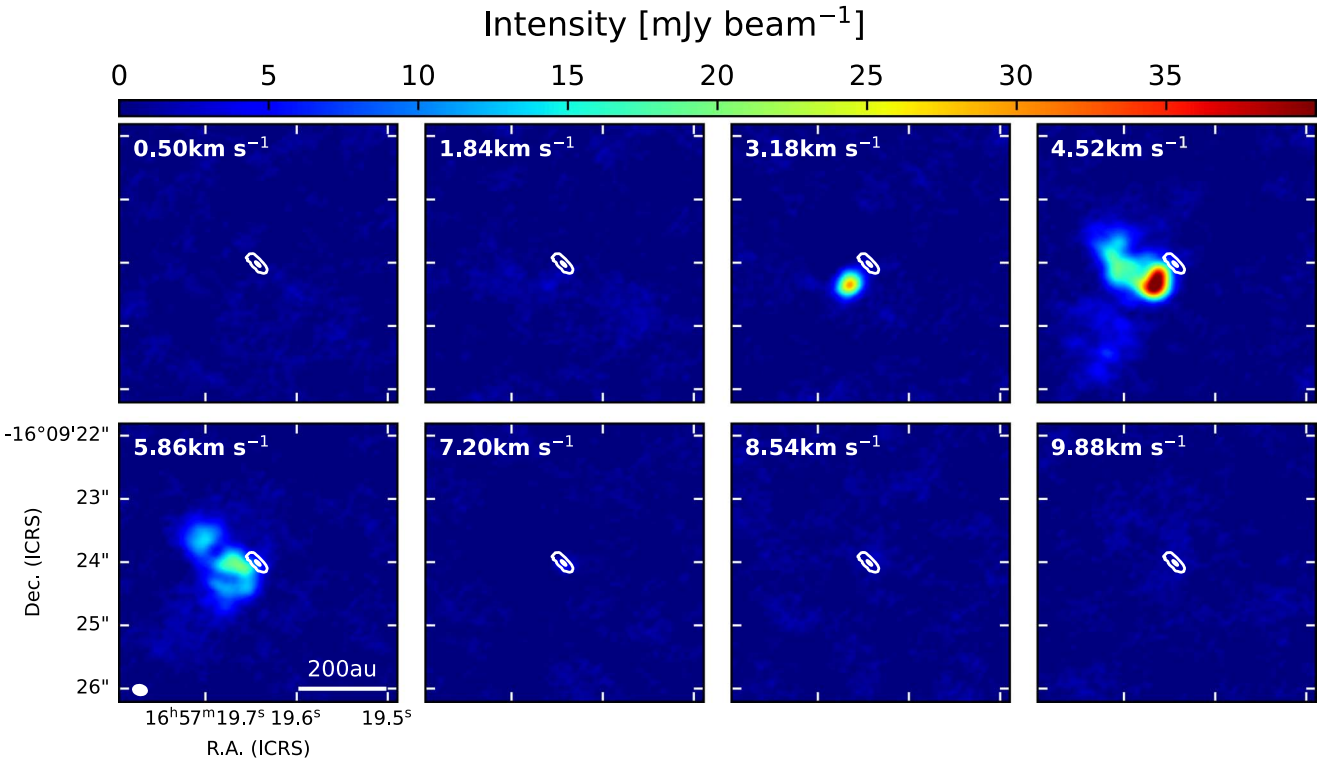

Figure A2. Velocity channel maps of the SiO (5–4) emission in IRAS 16544. Contours denote the distribution of the 1.3 mm dust continuum emission, and the contour levels are 5σ and 150σ (1$\sigma = 21$ μJy beam^{-1}).

transition peaks at the disk location. On the other hand, all three H_2CO transitions exhibit strong peaks toward the protostar. The H_2CO lines also trace the extended component surrounding the disk, and the $3_{0,3}$–$2_{0,2}$ transition also appears to trace the NE streamer. Multitransitional analysis using these three transitions of c-C_3H_2 and H_2CO should provide us with important insights on the physical conditions of the molecular gas, which should be the subject of subsequent papers.

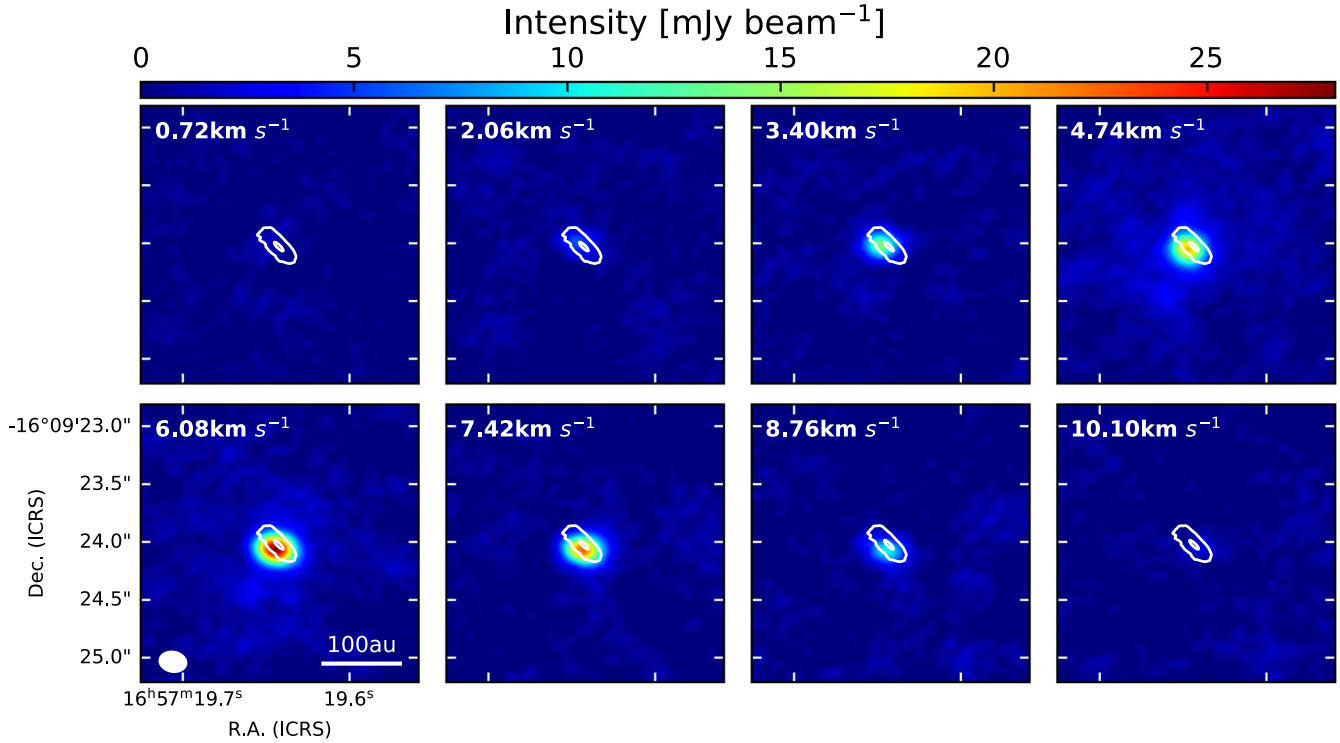

Figure A3. Velocity channel maps of the CH_3OH (4_2–3_1 E) emission in IRAS 16544. Contours denote the distribution of the 1.3 mm dust continuum emission, and the contour levels are 5σ and 150σ ($1\sigma = 21$ μJy beam^{-1}).

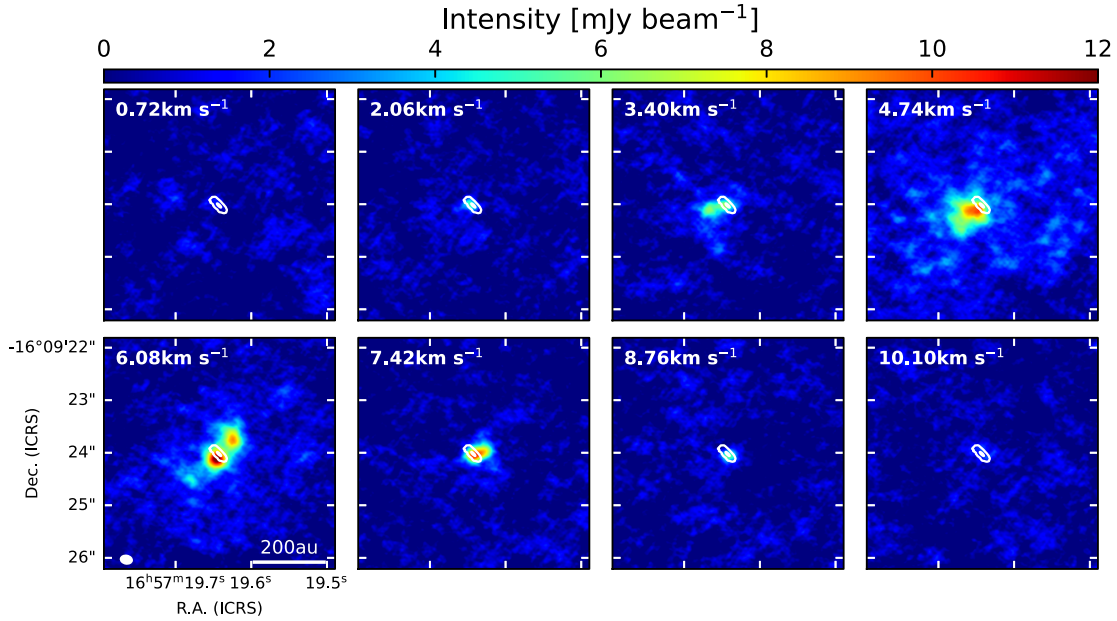

Figure A4. Velocity channel maps of the DCN (3–2) emission in IRAS 16544. Contours denote the distribution of the 1.3 mm dust continuum emission, and the contour levels are 5σ and 150σ ($1\sigma = 21$ μJy beam^{-1}).

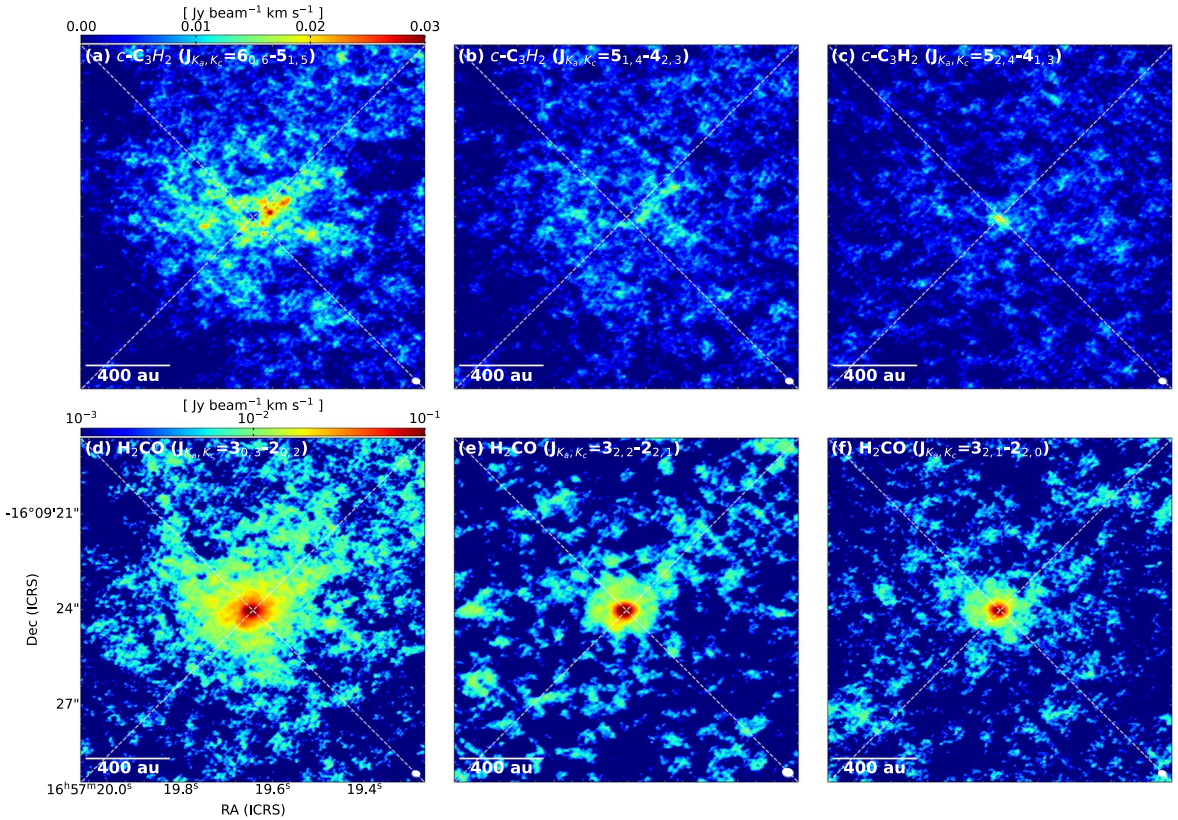

Figure A5. Moment 0 maps of the c-C_3H_2 (J_{K_a,K_c} = $6_{0,6}$–$5_{1,5}$; $5_{1,4}$–$4_{2,3}$; $5_{2,4}$–$4_{1,3}$) and H_2CO (J_{K_a,K_c} = $3_{0,3}$–$2_{0,2}$; $3_{2,2}$–$2_{2,1}$; $3_{2,1}$–$2_{2,0}$) emission as labeled. The integrated velocity ranges of the c-C_3H_2 ($6_{0,6}$–$5_{1,5}$; $5_{1,4}$–$4_{2,3}$; $5_{2,4}$–$4_{1,3}$) and H_2CO ($3_{0,3}$–$2_{0,2}$; $3_{2,2}$–$2_{2,1}$; $3_{2,1}$–$2_{2,0}$) emission are −0.62–18.14 km s^{-1}, −0.62–18.14 km s^{-1}, −0.62–18.14 km s^{-1}, −1.96–14.12 km s^{-1}, −1.96–15.46 km s^{-1}, and 0.01–10.03 km s^{-1}, respectively. The white dashed lines are the same as in Figure 4.

Appendix B
Velocity Channel Maps of the CO Isotopologue Lines

Figure B1 shows the full set of the velocity channel maps of the CO isotopologue lines in IRAS 16544, in both the entire and zoom-in regions (six images; Figure B1.1 to B1.6), is accessible through the online journal.

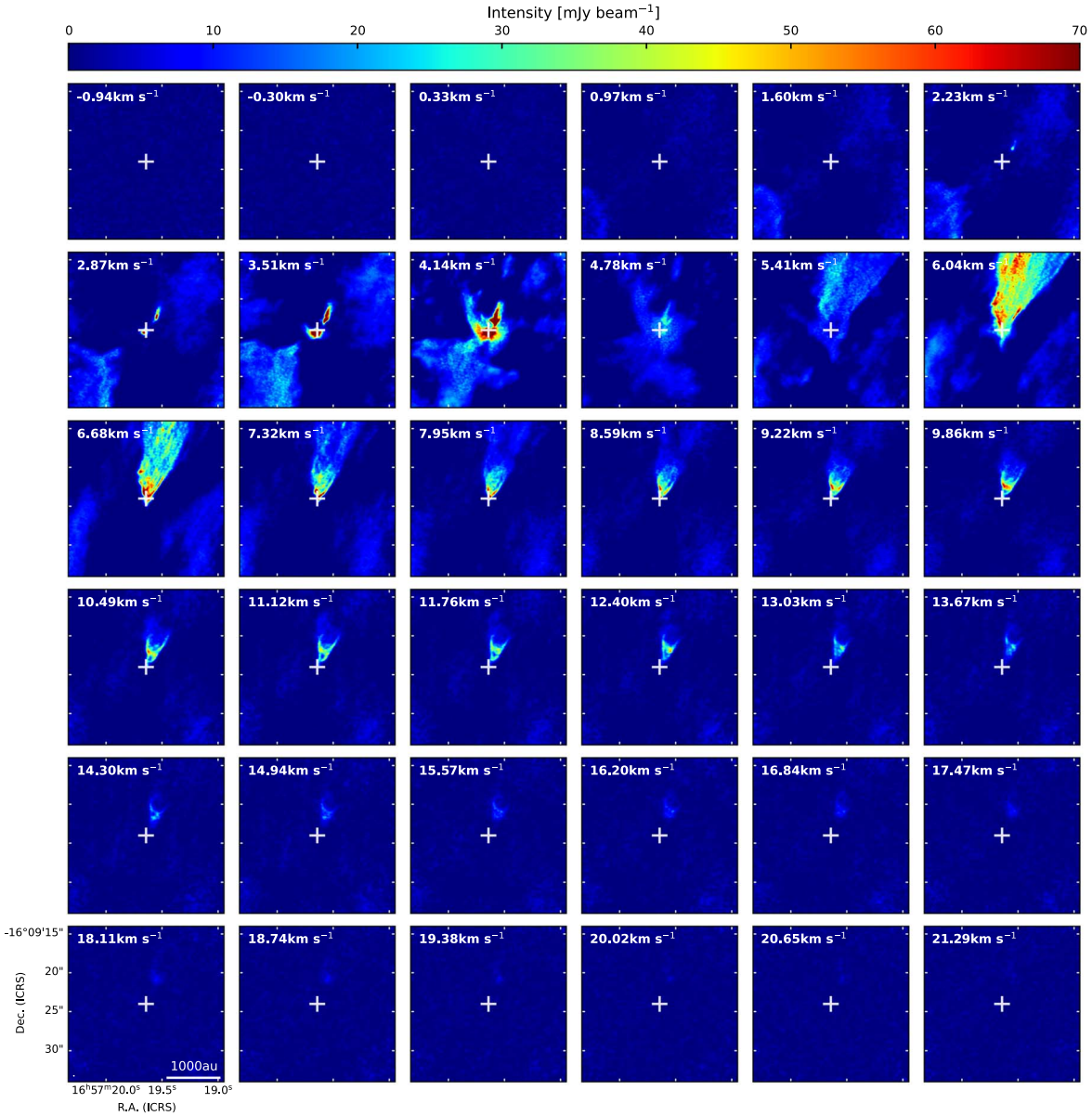

Figure B1. Velocity channel maps of the ^{12}CO (2–1) emission toward IRAS 16544 over the entire region. Crosses indicate the position of the protostar. A white ellipse in the lower left corner in the bottom left panel shows the synthesized beam. Velocity channel maps of the CO isotopologue lines Figure B1.1 to B1.6.

(The complete figure set (6 images) is available.)

ORCID iDs

Miyu Kido https://orcid.org/0000-0002-2902-4239
Shigehisa Takakuwa https://orcid.org/0000-0003-0845-128X
Kazuya Saigo https://orcid.org/0000-0003-1549-6435
Nagayoshi Ohashi https://orcid.org/0000-0003-0998-5064
John J. Tobin https://orcid.org/0000-0002-6195-0152
Jes K. Jørgensen https://orcid.org/0000-0001-9133-8047
Yuri Aikawa https://orcid.org/0000-0003-3283-6884
Yusuke Aso https://orcid.org/0000-0002-8238-7709
Frankie J. Encalada https://orcid.org/0000-0002-3566-6270
Christian Flores https://orcid.org/0000-0002-8591-472X
Sacha Gavino https://orcid.org/0000-0001-5782-915X
Itziar de Gregorio-Monsalvo https://orcid.org/0000-0003-4518-407X
Ilseung Han https://orcid.org/0000-0002-9143-1433
Shingo Hirano https://orcid.org/0000-0002-4317-767X
Patrick M. Koch https://orcid.org/0000-0003-2777-5861
Woojin Kwon https://orcid.org/0000-0003-4022-4132
Shih-Ping Lai https://orcid.org/0000-0001-5522-486X
Chang Won Lee https://orcid.org/0000-0002-3179-6334
Jeong-Eun Lee https://orcid.org/0000-0003-3119-2087
Zhi-Yun Li https://orcid.org/0000-0002-7402-6487
Zhe-Yu Daniel Lin https://orcid.org/0000-0001-7233-4171
Leslie W. Looney https://orcid.org/0000-0002-4540-6587
Shoji Mori https://orcid.org/0000-0002-7002-939X
Suchitra Narayanan https://orcid.org/0000-0002-0244-6650
Adele L. Plunkett https://orcid.org/0000-0002-9912-5705
Nguyen Thi Phuong https://orcid.org/0000-0002-4372-5509
Jinshi Sai (Insa Choi) https://orcid.org/0000-0003-4361-5577

Alejandro Santamaría-Miranda https://orcid.org/0000-0001-6267-2820
Rajeeb Sharma https://orcid.org/0000-0002-0549-544X
Patrick D. Sheehan https://orcid.org/0000-0002-9209-8708
Travis J. Thieme https://orcid.org/0000-0003-0334-1583
Kengo Tomida https://orcid.org/0000-0001-8105-8113
Merel L. R. van 't Hoff https://orcid.org/0000-0002-2555-9869
Jonathan P. Williams https://orcid.org/0000-0001-5058-695X
Yoshihide Yamato https://orcid.org/0000-0003-4099-6941
Hsi-Wei Yen https://orcid.org/0000-0003-1412-893X

References

ALMA Partnership, Brogan, C. L., Pérez, L. M., et al. 2015, ApJL, 808, L3
Andrews, S. M., Huang, J., Pérez, L. M., et al. 2018, ApJL, 869, L41
Arce, H. G., Shepherd, D., Gueth, F., et al. 2007, in Protostars and Planets V, ed. B. Reipurth, D. Jewitt, & K. Keil (Tucson, AZ: Univ. Arizona Press), 245
Aso, Y., Hirano, N., Aikawa, Y., et al. 2018, ApJ, 863, 19
Aso, Y., Hirano, N., Aikawa, Y., et al. 2019, ApJ, 887, 209
Aso, Y., Ohashi, N., Aikawa, Y., et al. 2017, ApJ, 849, 56
Aso, Y., Ohashi, N., Saigo, K., et al. 2015, ApJ, 812, 27
Aso, Y., & Sai, J. 2023, jinshisai/SLAM: First Release of SLAM, v1.0.0, Zenodo, doi:10.5281/zenodo.7783868
Astropy Collaboration, Price-Whelan, A. M., Lim, P. L., et al. 2022, ApJ, 935, 167
Bachiller, R., Codella, C., Colomer, F., Liechti, S., & Walmsley, C. M. 1998, A&A, 335, 266
Bachiller, R., Pérez Gutiérrez, M., Kumar, M. S. N., & Tafalla, M. 2001, A&A, 372, 899
Beckwith, S. V. W., Sargent, A. I., Chini, R. S., & Guesten, R. 1990, AJ, 99, 924
Bjerkeli, P., Ramsey, J. P., Harsono, D., et al. 2019, A&A, 631, A64
Cassen, P., & Moosman, A. 1981, Icar, 48, 353
Chini, R. 1981, A&A, 99, 346
Codella, C., & Muders, D. 1997, MNRAS, 291, 337
Czekala, I., Andrews, S. M., Jensen, E. L. N., et al. 2015, ApJ, 806, 154
Endres, C. P., Schlemmer, S., Schilke, P., Stutzki, J., & Müller, H. S. P. 2016, JMoSp, 327, 95
Ginsburg, A., Robitaille, T., & Beaumont, C. 2016, pvextractor: Position-Velocity Diagram Extractor, Astrophysics Source Code Library, ascl:1608.010
Hacar, A., & Tafalla, M. 2011, A&A, 533, A34
Hacar, A., Tafalla, M., & Alves, J. 2017, A&A, 606, A123
Hacar, A., Tafalla, M., Kauffmann, J., & Kovács, A. 2013, A&A, 554, A55
Hirano, N., Liu, S.-Y., Shang, H., et al. 2006, ApJL, 636, L141
Hirano, S., & Machida, M. N. 2019, MNRAS, 485, 4667
Hirano, S., Tsukamoto, Y., Basu, S., & Machida, M. N. 2020, ApJ, 898, 118
Hunter, J. D. 2007, CSE, 9, 90
Imai, M., Oya, Y., Sakai, N., et al. 2019, ApJL, 873, L21
Imai, M., Oya, Y., Svoboda, B., et al. 2022, ApJ, 934, 70
Kratter, K., & Lodato, G. 2016, ARA&A, 54, 271
Kuffmeier, M., Haugbølle, T., & Nordlund, Å. 2017, ApJ, 846, 7
Kuznetsova, A., Bae, J., Hartmann, L., & Mac Low, M.-M. 2022, ApJ, 928, 92
Launhardt, R., Evans, Neal, N. J. I., Wang, Y., et al. 1998, ApJS, 119, 59
Launhardt, R., & Henning, T. 1997, A&A, 326, 329
Launhardt, R., Nutter, D., Ward-Thompson, D., et al. 2010, ApJS, 188, 139
Lesur, G., Hennebelle, P., & Fromang, S. 2015, A&A, 582, L9
Li, Z.-Y., Krasnopolsky, R., Shang, H., & Zhao, B. 2014, ApJ, 793, 130
Lombardi, M., Lada, C. J., & Alves, J. 2008, A&A, 480, 785
Long, F., Pinilla, P., Herczeg, G. J., et al. 2018, ApJ, 869, 17
Matsumoto, T., & Tomisaka, K. 2004, ApJ, 616, 266
Maury, A. J., André, P., Testi, L., et al. 2019, A&A, 621, A76
McMullin, J. P., Waters, B., Schiebel, D., Young, W., & Golap, K. 2007, ASP Conf. Ser. 376, ed. R. A. Shaw, F. Hill & D. J. Bell (Tucson, AZ: Univ. Arizona Press), 127
Müller, H. S. P., Schlöder, F., Stutzki, J., & Winnewisser, G. 2005, JMoSt, 742, 215
Müller, H. S. P., Thorwirth, S., Roth, D. A., & Winnewisser, G. 2001, A&A, 370, L49
Murillo, N. M., Lai, S.-P., Bruderer, S., Harsono, D., & van Dishoeck, E. F. 2013, A&A, 560, A103
Ohashi, N., Saigo, K., Aso, Y., et al. 2014, ApJ, 796, 131
Ohashi, N., Tobin, J. J., Jørgensen, J. K. & eDisk Team 2023, ApJ, 951, 8
Okoda, Y., Oya, Y., Francis, L., et al. 2021, ApJ, 910, 11
Ortiz-León, G. N., Loinard, L., Kounkel, M. A., et al. 2017, ApJ, 834, 141
Oya, Y., Moriwaki, K., Onishi, S., et al. 2018, ApJ, 854, 96
Pascucci, I., Testi, L., Herczeg, G. J., et al. 2016, ApJ, 831, 125
Pineda, J. E., Segura-Cox, D., Caselli, P., et al. 2020, NatAs, 4, 1158
Pinte, C., Dent, W. R. F., Ménard, F., et al. 2016, ApJ, 816, 25
Robitaille, T. 2019, APLpy v2.0: The Astronomical Plotting Library in Python, Zenodo, doi:10.5281/zenodo.2567476
Robitaille, T., & Bressert, E. 2012, APLpy: Astronomical Plotting Library in Python, Astrophysics Source Code Library in Python, ascl:1208.017
Sakai, N., Sakai, T., Hirota, T., et al. 2014, Natur, 507, 78
Schöier, F. L., van der Tak, F. F. S., van Dishoeck, E. F., & Black, J. H. 2005, A&A, 432, 369
Sheehan, P. D., Tobin, J. J., Li, Z.-Y., et al. 2022, ApJ, 934, 95
Takakuwa, S., Saito, M., Lim, J., et al. 2012, ApJ, 754, 52
Takakuwa, S., Saito, M., Lim, J., & Saigo, K. 2013, ApJ, 776, 51
Teague, R. 2019, RNAAS, 3, 74
Teague, R., & Foreman-Mackey, D. 2018, RNAAS, 2, 173
Thieme, T. J., Lai, S.-P., Lin, S.-J., et al. 2022, ApJ, 925, 32
Tobin, J. J., Hartmann, L., Chiang, H.-F., et al. 2012, Natur, 492, 83
Tobin, J. J., Looney, L. W., Wilner, D. J., et al. 2015, ApJ, 805, 125
Tobin, J. J., Sheehan, P. D., Megeath, S. T., et al. 2020, ApJ, 890, 130
Tychoniec, L., Manara, C. F., Rosotti, G. P., et al. 2020, A&A, 640, A19
Tychoniec, L., Tobin, J. J., Karska, A., et al. 2018, ApJS, 238, 19
Ulrich, R. K. 1976, ApJ, 210, 377
Vallée, J. P., Bastien, P., & Greaves, J. S. 2000, ApJ, 542, 352
Vallée, J. P., & Fiege, J. D. 2007, AJ, 134, 628
van der Marel, N., Birnstiel, T., Garufi, A., et al. 2021, AJ, 161, 33
Ward-Duong, K., Patience, J., Bulger, J., et al. 2018, AJ, 155, 54
Wu, Y., Huang, M., & He, J. 1996, A&AS, 115, 283
Yen, H.-W., Gu, P.-G., Hirano, N., et al. 2019a, ApJ, 880, 69
Yen, H.-W., Koch, P. M., Takakuwa, S., et al. 2017, ApJ, 834, 178
Yen, H.-W., Takakuwa, S., Koch, P. M., et al. 2015, ApJ, 812, 129
Yen, H.-W., Takakuwa, S., Ohashi, N., et al. 2014, ApJ, 793, 1
Yen, H.-W., Zhao, B., Hsieh, I. T., et al. 2019b, ApJ, 871, 243
Zhao, B., Caselli, P., Li, Z.-Y., et al. 2016, MNRAS, 460, 2050
Zhao, B., Caselli, P., Li, Z.-Y., & Krasnopolsky, R. 2018, MNRAS, 473, 4868
Zucker, C., Speagle, J. S., Schlafly, E. F., et al. 2020, A&A, 633, A51